Kaya Mustafa Yücel (Orcid ID: 0000-0003-2966-5092)
Jepson Gilby (Orcid ID: 0000-0003-0151-3062)

Mesozoic–Cenozoic multistage tectonic evolution of the Pamir: detrital fission-track constraints from the Tajik Basin

Lin Li[1,2*], Yani Najman[3], Guillaume Dupont-Nivet[1,4], Mauricio Parra[5], Pierrick Roperch[1], Mustafa Kaya[6], Niels Meijer[7], Paul O'Sullivan[8], Gilby Jepson[2], Jovid Aminov[9]

[1]Géosciences Rennes-UMR 6118, CNRS-University of Rennes, Rennes, France

[2]Department of Geosciences, University of Arizona, Tucson, USA

[3]Lancaster Environment Centre, Lancaster University, Lancaster, UK

[4]Institute of Geosciences, Potsdam University, Potsdam, Germany

[5]Institute of Energy and Environment, University of São Paulo, São Paulo, Brazil

[6]Department of Geological Engineering, Middle East Technical University, Ankara, Türkiye

[7]Senckenberg Biodiversity and Climate Research Center (SBiK-F), Frankfurt, Germany

[8]GeoSeps Services, Moscow, Idaho, USA

[9]Institute of geology, earthquake engineering and seismology, Academy of Sciences, Dushanbe, Republic of Tajikistan

[*]Corresponding author email: li.lin8611@gmail.com; linli2@arizona.edu

Highlights:

- Pamir exhumation is interpreted from vitrinite reflectance, fission-track and U-Pb dating of Tajik Basin strata
- The Cimmerian orogeny (Late Triassic–Early Jurassic) and Neo-Tethyan subduction (mid-Cretaceous) were recorded
- Further exhumation during the Late Eocene–Neogene is associated with the Pamir's ongoing formation

This article has been accepted for publication and undergone full peer review but has not been through the copyediting, typesetting, pagination and proofreading process which may lead to differences between this version and the Version of Record. Please cite this article as doi: 10.1111/bre.12721

Abstract

Knowledge of the tectonic history of the Pamir contributes to our understanding of both the evolution of collisional orogenic belts as well as factors controlling Central Asian aridification. It is, however, not easy to decipher the Mesozoic–Cenozoic tectonics of the Pamir due to extensive Neogene deformation in an orogen that remains largely understudied. This study reports detrital apatite and zircon fission-track (FT) ages from both the eastern Tajik Basin sedimentary rocks and Pamir modern river sands. These FT data, supported by vitrinite reflectance and zircon and apatite U-Pb double dating, suggest that the majority of the FT ages are unreset and record exhumation stages of the Pamir, which has served as the source terrane of the Tajik Basin since the Cretaceous. Further, we combine the new data with a compilation of published detrital apatite and zircon FT data from both the Tajik Basin sedimentary rocks and Pamir modern river sands, to explore the Mesozoic–Cenozoic tectonic history of Pamir. Deconvolved FT Peak Ages document two major Mesozoic exhumation events associated with the Late Triassic–Early Jurassic Cimmerian orogeny that reflects accretion of the Pamir terranes, as well as the Early–early Late Cretaceous deformation associated with the northward subduction of the Neo-Tethys Ocean beneath Pamir. The compiled data also show significant Late Eocene–Neogene exhumation associated with the ongoing formation of the Pamir, which peaks at ~36 Ma, ~25 Ma, ~14 Ma, and ~7 Ma.

Keywords: Tajik Basin; Detrital fission-track; Double dating; Pamir tectonics; Mesozoic–Cenozoic; Exhumation

1. Introduction

Knowledge of Pamir evolution is important not only for understanding crustal deformation processes (Burtman and Molnar, 1993; Robinson, 2015; Rutte et al., 2017a; Sobel et al., 2013), but also for elucidating the impact of such processes on regional climate changes (Heermance et al., 2018; Wang et al., 2020). Significant advances have been made over the last two decades, both with regard to the deep structure (e.g., Kufner et al., 2021; Kufner et al., 2016; Schmidt et al., 2011; Schneider et al., 2013; Schwab et al., 2004; Sippl et al., 2013) and the geological evolution of the orogen (e.g., Robinson et al., 2004; Searle and Hacker, 2018; Stearns et al., 2013). However, major first-order questions remain unresolved to establish relationships between deep and surface processes and to understand the role of inherited Mesozoic structures on the Cenozoic Pamir evolution.

The Pamir consists of the North, Central, South Pamir, and Karakoram terranes (Fig 1). The latter three terranes are interpreted as fragments of Gondwana that drifted across the Tethys Ocean during the Mesozoic, subsequently docking with the southern margin of Asia, i.e., North Pamir (Angiolini et al., 2013; Robinson, 2015). Existing studies infer near synchronous closure of the Paleo-Tethys oceans which previously separated the different terranes of the Pamir, during the latest Triassic–Early Jurassic Cimmerian orogeny (Angiolini et al., 2013; Robinson, 2015). A phase of Mid-Cretaceous contractional deformation has also been inferred for the North and South Pamir, which was attributed to the northward subduction of the Neo-Tethys Ocean beneath the Pamir (Chapman et al., 2018a; Robinson, 2015). This inference is largely derived from explorations in the northeastern and southeastern Pamir. Other parts of the Pamir, especially the Central and western Pamir, may not share a similar Mid-Cretaceous tectonic history. For example, it has been inferred that the Central Pamir was at sea level during the Late Cretaceous (He et al.,

2018; Zhang et al., 2019). Documenting the existence and extent of these Mesozoic events and their ages is important to better understand the subsequent Cenozoic evolution. Detrital records provide unique opportunities to explore the tectonic history of source terranes for large areas.

Multiple deformation and exhumation stages have been proposed for the Cenozoic evolution of the Pamir. Based on low-temperature thermochronological data of bedrock in the northeastern Pamir, Amidon and Hynek (2010) identified two punctuated accelerated exhumation phases at 50–40 Ma and 25–16 Ma, respectively. Similarly, Sobel et al. (2013) proposed initiation of Cenozoic deformation and northward translation of the Pamir since ~25 Ma. Structural and thermochronological studies in the Central Pamir indicate intense contractional deformation during the Late Eocene and Late Oligocene (~35–22 Ma), followed by Early–Middle Miocene (20–12 Ma) exhumation of gneiss domes (Rutte et al., 2017a; Rutte et al., 2017b). Based on the observation of synchronous wetting and drying in the Tajik and Tarim basins, respectively, Wang et al. (2020) inferred that the Pamir probably reached significant elevations around 25 Ma. Furthermore, based on synchronous shifts of provenance and stable isotopes, Li et al. (2022) inferred a phase of deformation and surface uplift in the North Pamir since ~12 Ma, in line with coeval initiation of aeolian deposits in the Tarim Basin interpreted to reflect the closure of the wind gap between the Pamir and Tian Shan (Heermance et al., 2018). This study aims to further elucidate the protracted history of the formation of the `Pamir by identifying and dating exhumation events using low-temperature thermochronology on detrital records of the orogen.

Apatite and zircon fission-track dating record the cooling of the upper few kilometers (e.g., 3–10 km) of crust, and thus reflect its exhumation history (Gallagher et al., 1998). Unlike bedrock fission-track methods, which commonly record the most recent exhumation, detrital fission-track ages from stratigraphic successions record the evolving exhumation history of eroded rock units

in the hinterland, and thus may provide a much longer record of the source terrane exhumation (Garver et al., 1999; Ruiz et al., 2004). This study reports both detrital apatite and detrital zircon fission-track ages from a composite early Late Cretaceous–Late Miocene sedimentary section in the eastern Tajik Basin that has been recently dated using magnetostratigraphy (Kaya et al., 2020; Li et al., 2022), and from modern river sands from the western Pamir to complement existing source characterizations. Both fission-track and U-Pb methods were used to double date single grains in order to better evaluate exhumation signals. Vitrinite reflectance data was gathered to estimate burial temperature and assess potential resetting of the fission-track signal. Combined with published detrital fission-track data from both modern river sands from the Pamir and sedimentary rocks of the Tajik Basin, this study explores the Mesozoic–Cenozoic exhumation history of the Pamir.

2. Geologic background

2.1. Pamir

The Pamir-Karakoram is separated from the Alai Basin and Southwest Tian Shan by the Main Pamir thrust to the north, from the Tarim Basin by the Kashgar-Yecheng transfer system to the east, from the Tajik Basin by the Darvaz fault to the west, and from the Kohistan-Ladakh arc by the Shyok suture to the south (Fig. 1A). In the southeast and southwest, the Pamir connects to the Tibetan Plateau and the Hindu Kush, respectively (Fig. 1A). The North Pamir, Central Pamir, South Pamir, and Karakoram terranes are separated by the Tanymas suture, Rushan-Pshart suture, and Tirich-Mir boundary zone (TBZ) (Fig. 1A), respectively. The North Pamir can be further divided into the Oytag, Darvaz, and Karakul-Mazar terranes (Fig. 1A) (Rembe et al., 2021; Robinson et al., 2012; Schwab et al., 2004).

The Central Pamir, South Pamir, and Karakoram are all Gondwana-affiliated terranes, that drifted northward as one block toward the Eurasian continent during the Carboniferous–Permian (Angiolini et al., 2013; Robinson, 2015). During the Late Permian–Middle Triassic, rifting occurred between the Central and South Pamir, as well as between the South Pamir and Karakoram to create the Rushan Ocean and TBZ Basin (Angiolini et al., 2013; Robinson, 2015), both of which may represent narrow and never fully developed oceanic spreading centers (Leven, 1995; Zanchi and Gaetani, 2011). During the same period, the Paleo-Tethys ocean between the North and Central Pamir began to subduct northward to form the Karakul-Mazar magmatic complex (Schwab et al., 2004). The post-Middle Triassic tectonic evolution of the Pamir will be discussed in more detail later in this paper (e.g., section 6).

The modern Pamir is largely drained by the West-flowing Panj River into the Tajik Basin, and the tributaries of the Panj River drain the South, Central, and North Pamir (Fig. 1A). In contrast, only the easternmost part of the Pamir is drained by rivers into the Tarim Basin (Fig 1A). Due to this asymmetrical modern drainage configuration, and the argument that this asymmetrical configuration has existed at least since the Early Miocene (Carrapa et al., 2014), or even since the late Eocene (Jia et al., 2021), the Tajik Basin detritus, compared to detritus from the Tarim Basin, is more likely to record a comprehensive exhumation and tectonic history of the Pamir.

2.2. The Tajik Basin

The Tajik Basin is bounded by mountain belts on all sides, except its southwest corner: the Pamir to the east, the southwest Tian Shan to the north (Tajik Gissar) and northwest (Uzbek Gissar), and the Hindu Kush to the south (Fig. 1A). The Tajik Basin has probably been a foreland basin of the Pamir hinterland since the late Early Cretaceous (Chapman et al., 2020), or even since the late

Jurassic (Kaya et al., 2020); and thus has received detritus mainly shed from the different terranes of the Pamir during the Cretaceous and Cenozoic.

Internally, the Tajik Basin is characterized by north–south trending fold-thrust belts, which run parallel to the front of the Pamir hinterland, i.e., the Darvaz fault (Fig. 1A) (Chapman et al., 2017; Gągała et al., 2020). Shortening estimates of the fold-thrust belt vary significantly from ~65–70 km (Chapman et al., 2017), to ~93–148 km (Gągała et al., 2020), to ~240 km (Bourgeois et al., 1997). Low-temperature thermochronology studies yield relatively well-constrained ages for the initiation of the fold-thrust belt since ~16–12 Ma (Abdulhameed et al., 2020; Chapman et al., 2017). In addition to east–west shortening, the detached fold-thrust belts in the Tajik Basin also experienced counterclockwise rotations that decrease from the eastern basin (~60°) to the western basin (~0°) (Bazhenov et al., 1994; Pozzi and Feinberg, 1991; Thomas et al., 1994). The timing of the rotation, however, remains controversial due to poor age constraints in the basin (Bosboom et al., 2014; Thomas et al., 1994; Zhang and Sun, 2020).

2.3. Studied sections and age constraints

We collected detrital samples from a >4400 m long composite sedimentary section in the eastern Tajik Basin (Fig. 1B): the Khirmanjo (KH) and Shurobod (SB) sections, which were recently measured and dated in Kaya et al. (2020) and Li et al. (2022). These two sections cover a long succession from the late Early Cretaceous to the Late Miocene (Fig. 2). The lower ~700 m of the section is dominated by alluvial plain sandstones, with several intervals of coastal plain and tidal deposits of mudstones and sandstones (Kaya et al., 2020). Between 700 m and 1400 m, the rocks are dominated by marine tidal and carbonate ramp deposits, with intervals of coastal plain deposits (Kaya et al., 2020). The 1400–1600 m interval is a condensed section covering several

marine transgression and regression cycles. From 1600 m to the top of the section, the rocks are all terrestrial red-colored clastic rocks (Li et al., 2022): the 1600–2600 m interval is classified as the Baldshuan Formation, which includes three members: the fine-grained Shurisay Member (1600–1800 m), the conglomerate-dominated Kamolin Member (1800–1950 m), and the fine-grained Childara Member with numerous conglomerate interlayers (1950–2600 m); the Chingou Formation at the top of the section is dominated by conglomerates with mudstone intervals. Both the Baldshuan and Chingou formations are dominated by braided river deposits, with a small part of the Chingou Formation characterized by alluvial fan deposits (Li et al., 2022).

Stratigraphic ages of the KH and SB sections are constrained by both magnetostratigraphy and fossil assemblages (Fig. 2) (Kaya et al., 2020; Li et al., 2022). Deposition of these two sections started in the late Early Cretaceous (ca. 110 Ma), with a major hiatus between 37 and 20 Ma, and lasted until ~8 Ma (Fig. 2). The depositional ages of detrital samples collected from the Baldshuan and Chingou formations are relatively well constrained with small uncertainties (<0.5 Ma) (Li et al., 2022), while detrital samples collected from the lower marine sections have generally larger uncertainties up to a few million years (Kaya et al., 2020).

3. Methods

3.1. Samples

Four different types of samples were analyzed for this study (Table 1): 1) Twelve detrital sandstone samples from the KH and SB sections for detrital apatite double dating (fission-track and U-Pb; 11 of the 12 samples) and/or detrital zircon fission-track (6 of the 12 samples) analysis; 2) Two granite clasts from the Baldshuan Formation conglomerates for zircon U-Pb and fission-track analysis; 3) Four modern sand samples from tributaries of the Panj River (Obikhumbou, Vanj,

Yazgulom, and Bartang) draining the Pamir for detrital apatite double dating (on all 4 samples) and/or detrital zircon fission-track (on 3 of the 4 samples) analysis; 4) Four black shale samples from the Cretaceous strata of the KH section for vitrinite reflectance analysis. Detrital samples were processed using standard mineral separation techniques including gravity, heavy liquid, and magnetic separations to separate and concentrate zircon and apatite grains at both Potsdam University (Germany) and the University of Rennes (France).

3.2. Apatite fission-track and U-Pb double dating

3.2.1. Laboratory analyses

Apatite fission-track (AFT) and U-Pb double dating was performed at GeoSep Services (Idaho, USA) using standard procedures for the laser-ablation inductively-coupled plasma mass spectrometer (LA-ICPMS) method. See Supplementary Text S1 as well as Donelick et al. (2005) for a full description of analytical procedures. Supplementary Tables S1 and S2 record raw data for apatite FT and U-Pb measurements, respectively.

3.2.2. Data processing

To obtain the most reliable apatite fission-track data, we adopted the following processing steps: First, as apatite with low uranium content [U] yields low spontaneous fission-track densities, the revealed tracks can differ significantly depending on the surface etched. We thus excluded apatite with [U] content lower than 2 ppm. Second, two different U content parameters were measured with the LA-ICPMS method (see Supplementary Table S1): $^{238}U/^{43}Ca$ and [U] (ppm). Theoretically, these two parameters should exhibit a linear relationship with a [U]/($^{238}U/^{43}Ca$) slope of ~190 (Donelick et al., 2005). We considered as acceptable a deviation of ±25% in this slope. Thus, a linear test was enforced to exclude analyses with [U]/($^{238}U/^{43}Ca$) slopes smaller than

142.5 or larger than 237.5. Third, analyses with standard errors larger than 75% of the analyzed values were excluded. Lastly, we also excluded zero-track grains for the purpose of deconvolving the Peak Ages. All four criteria were enforced during data processing for the following discussion.

The pooled age and central age, both of which define the "average" age of a group of single-grain FT ages, are routinely calculated for bedrock samples, which record a single cooling event. However, these ages are meaningless for detrital samples with $P(\chi^2)$ close to 0, as when the *P*-value is lower than 0.05, it indicates that the single-grain FT ages are over-dispersed, and multiple age components exist (Vermeesch, 2019). We, therefore, used the mixture modeling of online software *IsoplotR* (*http://isoplotr.geol.ucsb.edu/isoplotr/)* (Vermeesch, 2018) to deconvolve single-grain FT ages of each sample into multiple age components, which are defined as Peak Ages.

Due to the low content of [U], many apatite grains did not yield U-Pb ages or yielded ages with very large errors (Supplementary Table S2). We filtered the apatite U-Pb age data to only include analyses with 2-sigma errors smaller than 75% of the U-Pb age.

3.3. Zircon fission-track and U-Pb dating

3.3.1 Zircon fission-track dating

Zircon fission-track (ZFT) analysis was performed following the external detector method (Gleadow, 1981) at the Low-Temperature Thermochronology Laboratory at the University of Sao Paulo (Brazil). See Supplementary Text S2 for a full description of analytical procedures and Supplementary Table S3 for the raw data of analyzed samples.

All the raw data were filtered using the standard error criteria, and all reported single-grain ZFT ages pass this test. As the $P(\chi^2)$ is close to 0 for all ZFT samples, we used the same Peak Age deconvolution method as for the AFT samples described above.

3.3.2 Zircon U-Pb dating

Zircon U-Pb dating was carried out using a Thermo Element 2 single collector inductively coupled plasma-mass spectrometer (LA-ICPMS) coupled to a Photon Machines Analyte G2 excimer laser at the Arizona LaserChron Center,University of Arizona (USA) following the method outlined by Gehrels et al. (2008). See Supplementary Text S3 for a full description of analytical and data processing procedures and Table S4 for raw data of analyzed samples.

3.4. Compilation of regional detrital fission-track data

3.4.1. Data sources

In the Tajik Basin and adjacent Pamir, fission-track ages of both detrital and bedrock samples have been published (e.g., Abdulhameed et al., 2020; Carrapa et al., 2014; Chapman et al., 2017; Rutte et al., 2017a; Sobel and Dumitru, 1997; Stübner et al., 2013; Thiede et al., 2013; Wang et al., 2019). To explore the long-term exhumation history of the Pamir, we compiled the following detrital fission-track data sets (see Fig. 1 for locations): 1) detrital apatite FT data of modern river sands from the Pamir (Carrapa et al., 2014); 2) detrital apatite FT data from the PE section (30–23 Ma) of the north-central Tajik Basin (Wang et al., 2019); and 3) detrital zircon FT data from the DH section of the eastern Tajik Basin (Chapman et al., 2020). These data sets were combined with the new AFT and ZFT data of this study for further analysis (section 3.4.2). Detrital fission-track data have also been reported from the southwestern Tarim Basin (e.g., Cao et al., 2015; Cao et al., 2013b; Clift et al., 2017; Wang et al., 2021). We did not incorporate these data in the compilation

because a significant component of the detritus in these Tarim sections was sourced from the West Kunlun to the south, thus yielding information that may not be directly relevant to the Pamir.

3.4.2. Data processing

To extract the most useful information from the compiled FT ages, we evaluated two different strategies of data processing: either compiling all the single-grain FT ages in Kernel Density Estimate (KDE) plots; or, compiling all the deconvolved Peak Ages to make KDE plots. We chose the second strategy for the following reasons: Single-grain FT ages are not as meaningful as single-grain ages from other methods, such as zircon U-Pb, due to the intrinsic characteristics of FT accumulation resulting in a Poissonian distribution of fission tracks in a crystal (Galbraith, 1981). Thus, for bedrock, a "pooled age" is usually used to represent the cooling age; while for detrital samples, each deconvolved Peak Age represents a distinct cooling age in the source terranes (e.g., Vermeesch, 2019). As a result, a compilation of Peak Ages is more meaningful than a compilation of single-grain ages to represent the source terrane cooling ages. Peak Ages that indicate partial annealing, such as those of the two Cretaceous samples from the KH section, amongst others (see detailed discussion in section 5.1), were excluded from the compilation, as these Peak Ages do not represent exhumation ages.

The original AFT data of Carrapa et al. (2014) and the ZFT data of Chapman et al. (2020) were reprocessed to derive the deconvolved Peak Ages. As individual Peak Ages may be interpreted to reflect source terrane cooling events (Garver et al., 1999; Ruiz et al., 2004), we plotted the KDE curves for the compiled AFT and ZFT Peak Ages to reflect the intensity and contribution of individual cooling events, similar to common interpretations of detrital zircon U-Pb provenance. The height of the KDE plot peak arguably reflects the intensity of corresponding Peak Ages in the source terrane, i.e., higher KDE peaks indicate stronger cooling events, either

regionally more extensive or temporally more intensive, similar to the interpretation of bedrock FT age KDE plots in Jepson et al. (2021).

Unlike bedrock FT ages, an issue that needs to be considered when constructing the KDE plots of compiled detrital FT Peak Ages from multiple samples, is the treatment of individual Peak Ages. Each sample considered will have deconvolved Peak Ages represented by a variable number of single-grain ages. Also, Peak Ages defined by a percentage of grains within a sample may represent very different numbers of grains between samples because the total number of analyzed grains differs between samples. Two different ways of accounting for individual Peak Ages can thus be considered. We can simply ignore the percentage represented by each individual Peak Ages in each sample and treat each Peak Age with the same weight when constructing the KDE plots. However, this strategy may over-represent Peak Ages that only occupy a small percentage in each sample. Alternatively, we can determine different weights for different Peak Ages according to their incorporated single-grain age percentage in each sample and treat the weight of each sample the same. Each Peak Age was weighted by values obtained as follows: in each sample, we first divided the percentage of each Peak Age by ten and then rounded the value to their nearest integer. This integer was considered as the weight of the Peak Age. Each Peak Age was then counted multiple times by its weight for the construction of the KDE plots. We consider that this second strategy better represents the source terrane cooling ages, and therefore it was adopted in the following analyses and discussion.

3.5. Vitrinite reflectance analysis

Vitrinite reflectance is the proportion of incident light reflected from a polished vitrinite surface (%Ro), which is a proxy of the thermal maturity of organic matter (Taylor et al., 1998).

Adopting certain transfer equations, vitrinite reflectance values can be converted to burial temperatures (e.g., Barker and Goldstein, 1990; Nielsen et al., 2017; Sweeney and Burnham, 1990). Four organic-rich shale samples were collected from the Cretaceous marine strata of the KHC section (Fig. 2). The analyses were carried out at the Federal University of Rio Grande do Sul (Brazil). Samples were processed following standard procedures (Bustin et al., 1985) to make plugs for vitrinite reflectivity measurement according to ISO standard 7404-5 (*https://www.iso.org/obp/ui/#iso:std:iso:7404:-5:ed-3:v1:en*). For each sample, 34 to 51 measurements were made. Following Abdulhameed et al. (2020), we converted the %Ro values to burial temperatures using two different methods: an empirical equation from Barker and Goldstein (1990), and a chemical kinetic model equation from Sweeney and Burnham (1990).

4. Results

4.1. New apatite fission-track ages

All AFT samples fail the χ^2 test, with $P(\chi^2)$ values equal or close to 0 (Supplementary Fig. S1), indicating that these fission-track age distributions are mixtures of different cooling age components (Peak Ages). This is expected for not fully reset detrital FT samples (Ruiz et al., 2004). Significant differences exist concerning the deconvolved Peak Ages between modern river sands and sandstones (Table 2 and Fig. 3). Modern river sand samples are exclusively dominated by Late Oligocene–Early Miocene (P2) and Middle–Late Miocene (P1) populations. Sandstone samples from the KH and SB sections generally show three dominant Peak Age populations during the Early–early Late Cretaceous (P4), Late Cretaceous–early Paleogene (P3), and Late Eocene–Early Miocene (P2), but also with a few Middle–Late Miocene (P1) and Late Jurassic (P5) populations.

We emphasize that the deconvolved Peak Ages only change slightly when using different filtering methods as discussed in section 3.2.2, e.g., adopting no filters, or only adopting [U] content and zero-track filters. The differences between deconvolved Peak Ages are small (Supplementary Fig. S2) and exert no influence on the following interpretation and discussion.

4.2. New zircon fission-track ages

Similar to the AFT ages, the ZFT ages of all samples have $P(\chi^2)$ values equal or close to 0 (Supplementary Fig. S3), indicating mixtures of different cooling age components (Peak Ages). In contrast to the exclusively young AFT Peak Ages, the ZFT ages of modern river sand samples shares similar Peak Age populations to sandstone samples (Table 3 and Fig. 4). In general, there are strong Triassic–Early Jurassic (P5), Early–early Late Cretaceous (P4), Late Cretaceous–early Paleogene (P3), and Late Eocene–Early Miocene (P2) populations, while the Middle–Late Miocene population (P1) is less prominent.

As expected for a granite clast in which all the grains experienced a similar cooling history, the two granite clasts from the Baldshuan Formation conglomerates yielded single ZFT Peak Ages (Table 3). Sample TK18-44 (~14 Ma depositional age) recorded a single ZFT Peak Age of ~272 Ma, and sample TK18-45 (~18 Ma depositional age) recorded a single ZFT Peak Age of ~212 Ma.

4.3. New apatite and zircon U-Pb ages

The majority of apatite U-Pb ages are between 200 and 600 Ma, with another smaller cluster at 30–50 Ma. Due to large uncertainties, we do not discuss the geologic meaning of these single-grain apatite U-Pb ages, but compare them with the double-dated AFT ages in section 5.2.

Granite clast sample TK18-45 gave an unanchored zircon U-Pb age of 437 ± 7 Ma, and an anchored age of 447 ± 4 Ma (Supplementary Fig. S4). Both ages overlap within uncertainty at 443 Ma. Granite clast sample TK18-44 gave a surprising degree of variability of grain ages between 570–2644 Ma (Supplementary Fig. S4). In view of this uncertainty, we use this sample only as supporting evidence, given its single ZFT age (~272 Ma) is in agreement with that of granite clast TK18-45 (~212 Ma), thus supporting our conclusion regarding the timing of exhumation of the source terrane (section 6.1). Please see Supplementary Text S4 for further discussion of the two zircon U-Pb ages from these two samples.

4.4. Regional pattern of detrital fission-track ages

Generally, the Peak Ages of the compiled AFT and ZFT data agree with the new data reported in this study (Figs. 3–4), such that the modern river sand AFT Peak Ages are similar between the western and eastern Pamir rivers; and the ZFT Peak Ages are similar between the KH&SB sections and the DH section of the Tajik Basin (Figs. 3 and 4). Slightly different from the modern river sand AFT data of this study, the modern river sand AFT data reported by Carrapa et al. (2014) have several Mesozoic Peak Ages (Fig. 3); however, it is noted that the percentages of these old Peak Ages are small (e.g., <5%). The other notable differences include: 1) the AFT Peak Ages of the PE section sandstones are dominated by P2 and P3, lacking other Peak Ages (Fig. 3); and 2) the ZFT Peak Ages of the DH section sandstones lack P3 (Fig. 4).

The KDE plots of the compiled AFT and ZFT Peak Ages show several distinct peaks (Fig. 5A–B). For the AFT Peak Age KDE plot, there is a broad peak between 140 and 90 Ma and a strong peak between 40 and 6 Ma (Fig. 5A), the latter of which can be further subdivided into populations with sub-peaks at ~36 Ma, ~25 Ma, ~14 Ma, and ~7 Ma (Fig. 5C). The ZFT Peak Age

KDE plot shows four distinguishable peaks at 220–200 Ma, 110–90 Ma, 75–60 Ma, and 40–6 Ma (Fig. 5B), the latter of which also show distinct sub-peaks that are consistent with the populations identified from the AFT Peak Age KDE plot (Fig. 5D).

We also compared the KDE plots using the two different Peak Age processing methods discussed in section 3.4.2. The KDE plots show slight differences but possess the same peaks as discussed here (Supplementary Fig. S5).

4.5. Burial temperatures

The four vitrinite reflectance (%Ro) values show two groups (Table 4, and Supplementary Fig. S6). The two ~90 Ma samples have %Ro values of 0.44 and 0.50, corresponding to burial temperatures of 54–70 °C or 80–90 °C, depending on the different temperature calibration equations used (Table 4). The other two 97 Ma and 100 Ma samples have %Ro values of 0.61 and 0.67, corresponding to burial temperatures of 94–106 °C or 107–114 °C. A burial temperature reported adjacent to our KH section records 75 °C or 94 °C (depending on the two different transfer equations used in Abdulhameed et al., 2020), which is in between the values reported for our upper two and lower two samples in this study.

5. Evaluation of fission-track data

5.1. Influence of burial annealing

The closure temperature of the apatite fission-track system is ~120 °C, and fission tracks will anneal when residing in the partial annealing zone (PAZ) at ~120–60 °C (Green et al., 1989). Similarly, the closure temperature of the zircon fission-track system is ~240 °C, and the PAZ is from ~240–180 °C (Tagami, 2005). Deep burial of sedimentary rocks to their PAZ would reset the

primary cooling ages and yield fission-track ages that are useful to explore the thermal history of the basin but do not reflect the timing of exhumation of the grains' source region. Only samples that were shallowly buried and remained above the PAZ after deposition record the original exhumation information of the source terrane.

In the studied KH&SB and DH sections, all samples have their ZFT Peak Ages older than depositional ages (i.e., lag-time > 0 Ma; Fig. 6B). With one exception, all Cenozoic samples have their AFT Peak Ages older than depositional ages (Fig. 6A). We, therefore, interpret these Peak Ages as representing the timing of cooling in the source region. The one exception is TK16-11, the P1 of which is younger than its depositional age. We noted that this Peak Age only accounts for 6% of total single grain AFT ages, and a weak positive correlation was also observed between the single grain AFT ages and their Dpar values for this sample (Supplementary Fig. S7), indicating influence of chemical compositions of apatite grains on annealing temperatures (e.g., Peyton and Carrapa, 2013). We thus interpret this younger than depositional age AFT Peak Age as a result of the resetting of the AFT ages of certain apatite grains, i.e., those with smaller Dpar, which usually have slightly lower partial annealing temperatures (Ketcham et al., 1999).

For the two newly collected Cretaceous samples, all their AFT Peak Ages, except one, are younger than depositional ages (Fig. 6A). The presence of more than one Peak Age indicates partial rather than full resetting, which is consistent with vitrinite reflectance data that show burial temperatures of 54–90 °C for the Upper Cretaceous strata, and 94–114 °C for the upper Lower Cretaceous strata (Table 4, considering both transfer equations). These temperatures fall in the range of the AFT PAZ at ~120–60 °C. Both samples show a weak positive correlation of single grain AFT ages *vs.* Dpar, indicating an influence of mineral chemistry on age distribution (Carlson et al., 1999) (Supplementary Fig. S7).

5.2. Contribution of igneous cooling ages

To use detrital FT ages to reflect source terrane exhumation history, the contribution of volcanic and/or plutonic cooling ages should be first excluded, as these ages reflect the timing of shallow intrusion and/or eruption rather than exhumation. In the Pamir, Paleozoic to Eocene igneous rocks have been reported (Chapman et al., 2018b; Schwab et al., 2004). U-Pb and FT double dating on the same grain can help determine whether FT ages represent cooling post-eruption / shallow intrusion (similar U-Pb and FT ages) or are due to exhumation (U-Pb age older than FT age) (Reiners et al., 2005).

Fig. 7A shows that for the major exhumation periods that we will discuss in section 6, i.e., the Early–early Late Cretaceous and the Cenozoic, the majority of grains fall away from the apatite FT versus U-Pb 1:1 line, indicating that the FT ages represent exhumation signals (Reiners et al., 2005). In the DH section (Fig. 1), detrital zircon U-Pb and FT double dating from Chapman et al. (2020) (Fig. 7B) more clearly indicates exhumation signals, because the errors on zircon U-Pb analyses are much smaller than those for apatite.

5.3. Consideration of exhumation rates

From old to young (Fig. 6A–B), Peak Age populations P5 (Late Triassic–Early Jurassic), P4 (Early–early Late Cretaceous), and P3 (Late Cretaceous–early Paleogene), all have static peaks that show no changes in Peak Ages but increasing lag times (Bernet and Garver, 2005). For P2 of the AFT data, the majority of lag times have values that range between 8–14 Myrs, with an average of 10 Myrs for the Miocene sedimentary rocks (Fig. 6A and Table 2). The lag times of P2 on the ZFT plot (Fig. 6B) are more scattered, mainly between 10–15 Myrs. P2 may represent a moving

peak of constant lag time (Fig. 6A–B), indicating steady state exhumation during the Miocene, perhaps with accelerated exhumation to the present as indicated by shorter lag times of some P1 modern river sediments. However, this suggestion should be viewed with caution, given that peaks represent input from more than one terrane, and thus can only represent a spatially averaged scenario.

Assuming a thermal gradient of ~25 °C/km, the long-term exhumation rate in the Pamir during the Miocene, deduced from the compiled detrital FT data of this study, is ~0.5–1 mm/yr, which generally agrees with the estimated average Cenozoic exhumation rates of 0.6–1.3 mm/yr in the Central and South Pamir, but higher than the 0.4–0.2 mm/yr rates for the Northeastern Pamir, based on bedrock ^{40}Ar-^{39}Ar dating (Carrapa et al., 2014).

There is one sample (TK16-14, Table 2) showing ~1 Myr AFT lag time (AFT Peak Age 1: ~17.2 Ma; depositional age: ~16.3 Ma). Early Miocene crystallization ages (21–16 Ma) were reported from leucogranite from the Pamir gneiss domes (Chapman et al., 2018b; Stearns et al., 2015), hinting that the 17.2 Ma AFT Peak Age may represent igneous cooling and/or volcanic extrusion age. Further examination of single grain apatite FT and U-Pb ages indicates that this is not the case as the majority of grains incorporated in this Peak Age are much older than 25 Ma (Supplementary Fig. S8). We, thus, interpret this very short lag time to represent very high exhumation rate (~4–5 mm/yr) at 17–16 Ma. Exhumation rates as high as >3 mm/yr and 1–3 mm/yr were reported from the Central and South Pamir gneiss domes, respectively, both of which are active since ~20 Ma (Rutte et al., 2017a; Stübner et al., 2013). This is also consistent with exhumation rate estimates from modern river sand detrital thermochronology (Carrapa et al., 2014). The fact that this very short lag-time was only found in one of the samples argues for the short duration of the ~17–16 Ma intense exhumation event represented by this Peak Age.

6. Mesozoic–Cenozoic tectonic evolution and formation of the Pamir

6.1. Provenance of the grains dated by fission-track analyses

As argued in the last section (5), the deconvolved Peak Ages of detrital fission-track samples reflect the long-term exhumation history of the source terranes. Before discussing the exhumation history, we first need to identify the source terranes of these apatite and zircon grains. In the eastern Tajik Basin, including the DH, SB, and KH sections, provenance studies, including the use of the detrital zircon U-Pb method, indicate that the Pamir has served as the major detrital source since the Cretaceous (Chapman et al., 2020; Kaya et al., 2020; Klocke et al., 2017; Li et al., 2022; Wang et al., 2019). Further refinement of our discussion can be attained by determination of which terranes in the Pamir sourced the grains.

Leaving aside any issues of potential recycling, modern river sands are the easiest to interpret in this respect, since the source is clear (Fig. 1A), but only provides a modern-day snapshot. Interpretation of detrital samples from older strata is possible where characteristics differ between potential source regions. In the Pamir, Triassic and Paleozoic granites are typical of the North Pamir, Eocene intrusions are typical of the Central Pamir, and Cretaceous intrusions are typical of the South Pamir (Chapman et al., 2018b; Schwab et al., 2004). Our granite conglomerate clasts (samples TK18-44 and 45) are Paleozoic, as determined from zircon U-Pb dating (section 4.3) and we therefore consider them derived from the North Pamir. Double-dated individual grains in the sandstone sections cannot be so readily assigned to a specific terrane since grains from the igneous rocks may have been eroded, transported, and redeposited in sediments on a different terrane; for example, Central and South Pamir Mesozoic sedimentary rocks have a Triassic zircon population although Triassic igneous rocks are not present in this terrane (Li et al., 2022; Villarreal et al.,

2020). However, there are limited sedimentary rocks younger than Jurassic in the North Pamir and therefore we are confident to ascribe grains with Cretaceous and Eocene U-Pb ages to the South and Central Pamir, respectively. Eocene grains are recorded in both the KH&SB and DH sections; Cretaceous grains are rare, although the KH section show a few zircons (Fig. 7).

6.2. Late Triassic–Early Jurassic Cimmerian orogeny in the Pamir

Our new ZFT data, and almost all the compiled detrital ZFT samples show Late Triassic–Early Jurassic Peak Ages (P5: 170–230 Ma; Fig. 4). On the KDE plot of the compiled ZFT Peak Ages, a peak between 200–230 Ma can also be identified (Fig. 5B). From provenance information, we know that this period of exhumation affected the North Pamir as determined by the Triassic FT ages of the granite conglomerate clasts, and the Central and/or South Pamir as determined from ZFT ages in the modern river sands of the Bartang and possibly also the Vanj rivers which drain the Central and South Pamir (Fig. 1), although the Triassic Peak Age in the latter has large errors (Table 3).

Previous studies, which used stratigraphy, geochronology, thermochronology, provenance, and structural methods, inferred broadly synchronous terrane collisions between the North, Central, South Pamir, and Karakoram during the latest Triassic–earliest Jurassic (Angiolini et al., 2013; Imrecke et al., 2019; Robinson, 2015; Villarreal et al., 2020). We thus interpret these Late Triassic–Early Jurassic FT cooling ages to record the exhumation associated with the closure of the Paleo-Tethys Ocean and the ensuing terrane collisions which caused strong deformation along the Tanymas and Rushan-Pashart suture zones during the Cimmerian orogeny.

Late Triassic cooling ages have also been documented by detrital samples from the Tian Shan, which was also interpreted to be associated with the Cimmerian collision in the southern

Eurasian margin (De Grave et al., 2012). Similar Late Triassic–Early Jurassic detrital zircon FT ages from the West Kunlun, however, were interpreted to reflect the northward subduction of the Paleo-Tethys oceanic lithosphere beneath the West Kunlun (Cao et al., 2015).

6.3. Early–early Late Cretaceous rejuvenated deformation in the Pamir

Both AFT and ZFT Peak Ages show strong Early–early Late Cretaceous exhumation signals (P4; Figs. 3–4). The KDE plots show subtle differences between the compiled AFT and ZFT data (Fig. 5): the AFT Peak Age KDE plot has a relatively broad range between 140 Ma and 90 Ma, while the ZFT Peak Age KDE plot has a narrower range between 110 Ma and 90 Ma.

We interpret these cooling ages to record exhumation associated with rejuvenated deformation in the Pamir during the Early–early Late Cretaceous. Multiple lines of evidence support this interpretation. In the northeast Pamir, it is inferred that during the Early–early Late Cretaceous, the Karakul-Mazar terrane was imbricated by thrust faults and over-thrusted southward above the Central Pamir (Robinson et al., 2012; Rutte et al., 2017b). Amphibolite facies metamorphism in the Karakul-Mazar terrane was interpreted to be caused by thrust imbrication (Robinson et al., 2004). Thick Cretaceous fluvial rocks in the Tarim and Tajik Basins were interpreted to be deposited in foreland basins and sourced from the Karakul-Mazar terrane (Bershaw et al., 2012; Chapman et al., 2020; Kaya et al., 2020). In the South Pamir, mapping and thermochronology studies document Cretaceous shortening and exhumation (cooling ages: 110–80 Ma) (Chapman et al., 2018a).

Based on the observation of synchronous deformation and exhumation in the North and South Pamir, Robinson (2015) suggested that the entire Pamir experienced Early–early Late Cretaceous deformation. During the same time interval, Cretaceous arc magmatism (South Pamir

Batholith) occurred in the South Pamir (Aminov et al., 2017; Chapman et al., 2018a). It is thus inferred that the Early–early Late Cretaceous arc magmatism and retro-arc deformation and exhumation in the Pamir were caused by the northward subduction of the Neo-Tethys oceanic lithosphere beneath the Pamir crust (Robinson, 2015). This slab subduction inference seems to be consistent with the suggestion from studies in Tibet that the Neo-Tethys ocean ceased slab rollback and resumed its advance since ~120 Ma, and lasted until ~90 Ma (Kapp and DeCelles, 2019). The strong 110–90 Ma peak of the compiled ZFT Peak Age KDE plot (Fig. 5B) corresponds to the initiation of strong arc magmatism (110–90 Ma, peak at ~104 Ma) in the South Pamir (Aminov et al., 2017; Chapman et al., 2018a), probably suggesting a phase of intense subduction of the Neo-Tethys Ocean. This stage of contractional deformation may have also influenced the Tian Shan and West Kunlun area to cause Early Cretaceous rapid cooling there (Cao et al., 2015; Dumitru et al., 2001; Jepson et al., 2018).

From the above, it can be deduced that it is likely that all Pamir terranes were exhuming during this period, although direct evidence for the exhumation of the Central Pamir during this interval has remained elusive. Our modern river ZFT data from the Obikhumbou River draining the North Pamir (TK16-35, Table 3) shows evidence for this phase of exhumation whilst our data from the modern Vanj River (TK16-36) draining the Central Pamir does not. However, such exhumation is hinted at in the Vanj River (TJK8, Table 2) and Gunt River (TJK5) AFT data from Carrapa et al. (2014), which drain the Central Pamir and South Pamir, respectively. Considering the complications of potential recycling of sandstone samples, further ZFT studies of modern river sands from the Central Pamir are needed to more robustly verify whether this Early–early Late Cretaceous exhumation occurred in the Central Pamir.

6.4. Late Eocene–Neogene formation of the Pamir

The most prominent peak of the compiled AFT Peak Age KDE plot (Fig. 5A) and the second most prominent peak of the compiled ZFT Peak Age KDE plot (Fig. 5B) is the one in the Cenozoic (e.g., 40–0 Ma). The compiled number of grains contributing to the ZFT Peak Ages is small, which may generate unreliable peaks on the KDE plot. We thus focus the following discussion mainly on AFT ages, but also taking into consideration the ZFT ages.

Mainly based on the AFT data, we identified four populations within the 40–0 Ma range with peaks at ~36 Ma, ~25 Ma, ~14 Ma, and ~7 Ma (Fig. 5C). The first three populations are also recorded by ZFT ages (Fig. 5D), while the last population is only recorded in the AFT ages of modern river sand samples (Table 2). This suggests that the last stage of exhumation has not yet eroded deep enough to expose rocks with Late Miocene ZFT ages to the surface. Modern river FT data show that the four exhumation stages we identified are present in the North, Central, and South Pamir (Tables 2 and 3).

Our results agree with previous studies documenting Late Eocene–Neogene deformation and exhumation in the Pamir. A Late Oligocene–Early Miocene growth phase of the Pamir has been documented widely in sedimentary records in the surrounding basins (Tajik, Tarim, and Alai) (Blayney et al., 2019; Coutand et al., 2002; Wang et al., 2019). The Middle–Late Miocene exhumation in the Pamir is also echoed in studies that include the appearance of thick conglomerate deposits at 15 Ma and 13.5 Ma in the Tarim and Tajik basins, respectively (Blayney et al., 2019; Li et al., 2022; Zheng et al., 2015) and a significant provenance shift from the Central to the North Pamir denoting a phase of exhumation around 12 Ma (Li et al., 2022).

Within the Pamir, significant crustal thickening occurred in the Central Pamir during the Late Eocene and Early Miocene (e.g., >37 Ma to ~20 Ma), which caused prograde metamorphism

recorded in Miocene gneiss domes across the region and led to the present-day crustal thickness of ~70 ± 10 km (Hacker et al., 2017; Rutte et al., 2017a). Shortly after, significant exhumation of the gneiss domes from middle–lower crustal levels prevailed in the Central Pamir from ~22 Ma until ~12 Ma and until ~4 Ma in the South Pamir (Rutte et al., 2017a; Stübner et al., 2013; Worthington et al., 2020). The Central Pamir dome exhumation possibly reflects the very short lag-time at ~17–16 Ma observed in one of our samples (Fig. 6A). In the northeastern Pamir, bedrock experienced a stage of accelerated exhumation at 25–16 Ma (Amidon and Hynek, 2010; Sobel et al., 2013), and another stage in the Late Miocene–Pliocene associated with the Kongur Shan extensional system (Cao et al., 2013a; Chen and Chen, 2020; Robinson et al., 2004; Sobel et al., 2011; Thiede et al., 2013). In the northwestern Pamir, bedrock AFT ages between 15 Ma and 6 Ma, and zircon and apatite (U-Th)/He ages between 26 Ma and 2.5 Ma have also been reported (Abdulhameed et al., 2020; Sobel et al., 2021). AFT studies of modern river sands across the Pamir record strong Miocene–Pliocene signals indicating rapid erosion at the regional scale (Carrapa et al., 2014).

7. Conclusions

This study provides both apatite and zircon fission-track data from Cretaceous–Miocene sandstones from the eastern Tajik Basin and modern river sands from the Pamir to explore the Mesozoic–Cenozoic tectonic evolution and formation of the Pamir.

Vitrinite reflectance data and comparisons between FT ages and depositional ages indicate that the grains experienced negligible partial annealing except for the two lowermost samples in the Cretaceous part of the studied section, which were buried to their AFT partial annealing zone. Double dating further indicates that the majority of FT ages record mostly exhumation signals, and

do not represent the timing of shallow intrusion of igneous rocks or extrusion of volcanics. We thus interpret the fission-track data to record their source terrane long-term exhumation history.

A compilation of both the new AFT and ZFT data of this study and published detrital fission-track data from the Pamir and Tajik Basin show prominent Mesozoic cooling ages that reflect deformation and exhumation of the Pamir associated with the Late Triassic–Early Jurassic Cimmerian orogeny that collaged the Pamir terranes, as well as the rejuvenated Early–early Late Cretaceous deformation caused by the northward subduction of the Neo-Tethys oceanic lithosphere beneath Pamir. The compiled data set also shows strong exhumation of the Pamir during the Late Eocene–Neogene that peaks at ~36 Ma, ~25 Ma, ~14 Ma, and ~7 Ma.

Data Availability Statement:

The data that supports the findings of this study are available in the supplementary material of this article

Acknowledgments

We would like to thank Chris Mark for providing advice on processing the AFT ages, and Alex Pullen and Ian Millar on the processing of zircon U-Pb data. We thank Yanling Wang and Wai Allen for help with zircon BSE imaging and U-Pb analysis. We would like to thank Alexander Robinson, Xin Wang, and Editor Atle Rotevatn for constructive comments and suggestions that helped clarify the contents of this study. This study is supported by the European Research Council consolidator grant MAGIC 649081 to GDN.

References

Abdulhameed, S., Ratschbacher, L., Jonckheere, R., Gągała, Ł., Enkelmann, E., Käßner, A., Kars, M.S.C., Szulc, A., Kufner, S.K., Schurr, B., 2020. Tajik Basin and Southwestern Tian Shan, Northwestern India‐Asia Collision Zone: 2. Timing of Basin Inversion, Tian Shan Mountain Building, and Relation to Pamir‐Plateau Advance and Deep India‐Asia Indentation. Tectonics 39, doi: 10.1029/2019TC005873.

Amidon, W.H., Hynek, S.A., 2010. Exhumational history of the north central Pamir. Tectonics 29, doi:10.1029/2009TC002589.

Aminov, J., Ding, L., Mamadjonov, Y., Dupont-Nivet, G., Aminov, J., Zhang, L.-Y., Yoqubov, S., Aminov, J., Abdulov, S., 2017. Pamir Plateau formation and crustal thickening before the India-Asia collision inferred from dating and petrology of the 110–92 Ma Southern Pamir volcanic sequence. Gondwana Research 51, 310-326.

Angiolini, L., Zanchi, A., Zanchetta, S., Nicora, A., Vezzoli, G., 2013. The Cimmerian geopuzzle: new data from South Pamir. Terra Nova 25, 352-360.

Barker, C.E., Goldstein, R.H., 1990. Fluid-inclusion technique for determining maximum temperature in calcite and its comparison to the vitrinite reflectance geothermometer. Geology 18, 1003-1006.

Bazhenov, M.L., Perroud, H., Chauvin, A., Burtman, V.S., Thomas, J.-C., 1994. Paleomagnetism of Cretaceous red beds from Tadzhikistan and Cenozoic deformation due to India-Eurasia collision. Earth and Planetary Science Letters 124, 1-18.

Bernet, M., Garver, J.I., 2005. Fission-track analysis of detrital zircon. Reviews in Mineralogy and Geochemistry 58, 205-237.

Bershaw, J., Garzione, C.N., Schoenbohm, L., Gehrels, G., Tao, L., 2012. Cenozoic evolution of the Pamir plateau based on stratigraphy, zircon provenance, and stable isotopes of foreland basin sediments at Oytag (Wuyitake) in the Tarim Basin (west China). Journal of Asian Earth Sciences 44, 136-148.

Blayney, T., Dupont‐Nivet, G., Najman, Y., Proust, J.N., Meijer, N., Roperch, P., Sobel, E.R., Millar, I., Guo, Z., 2019. Tectonic evolution of the Pamir recorded in the western Tarim Basin (China): sedimentologic and magnetostratigraphic analyses of the Aertashi section. Tectonics 38, doi: 10.1029/2018TC005146.

Bosboom, R., Dupont-Nivet, G., Huang, W.T., Yang, W., Guo, Z.J., 2014. Oligocene clockwise rotations along the eastern Pamir: tectonic and paleogeographic implications. Tectonics 33, 53-66.

Bourgeois, O., Cobbold, P.R., Rouby, D., Thomas, J.C., Shein, V., 1997. Least squares restoration of Tertiary thrust sheets in map view, Tajik depression, central Asia. Journal of Geophysical Research: Solid Earth 102, 27553-27573.

Burtman, V.S., Molnar, P.H., 1993. Geological and geophysical evidence for deep subduction of continental crust beneath the Pamir. Geological Society of America special publication, 281, doi: 10.1130/SPE281-p1.

Bustin, R.M., Cameron, A.R., Grieve, D.A., Kalkreuth, W.D., 1985. Coal Petrology - its principles, methods, and applications. Geological Association of Canada, Victoria.

Cao, K., Bernet, M., Wang, G.-C., van der Beek, P., Wang, A., Zhang, K.-X., Enkelmann, E., 2013a. Focused Pliocene–Quaternary exhumation of the Eastern Pamir domes, western China. Earth and Planetary Science Letters 363, 16-26.

Cao, K., Wang, G.-C., Bernet, M., van der Beek, P., Zhang, K.-X., 2015. Exhumation history of the West Kunlun Mountains, northwestern Tibet: Evidence for a long-lived, rejuvenated orogen. Earth and Planetary Science Letters 432, 391-403.

Cao, K., Wang, G.-C., van der Beek, P., Bernet, M., Zhang, K.-X., 2013b. Cenozoic thermo-tectonic evolution of the northeastern Pamir revealed by zircon and apatite fission-track thermochronology. Tectonophysics 589, 17-32.

Carlson, W.D., Donelick, R.A., Ketcham, R.A., 1999. Variability of apatite fission-track annealing kinetics: I. Experimental results. American mineralogist 84, 1213-1223.

Carrapa, B., Mustapha, F.S., Cosca, M., Gehrels, G., Schoenbohm, L.M., Sobel, E.R., DeCelles, P.G., Russell, J., Goodman, P., 2014. Multisystem dating of modern river detritus from Tajikistan and China: Implications for crustal evolution and exhumation of the Pamir. Lithosphere 6, 443-455.

Chapman, J.B., Carrapa, B., Ballato, P., DeCelles, P.G., Worthington, J., Oimahmadov, I., Gadoev, M., Ketcham, R., 2017. Intracontinental subduction beneath the Pamir Mountains: Constraints from thermokinematic modeling of shortening in the Tajik fold-and-thrust belt. GSA Bulletin 129, 1450-1471.

Chapman, J.B., Carrapa, B., DeCelles, P.G., Worthington, J., Mancin, N., Cobianchi, M., Stoica, M., Wang, X., Gadoev, M., Oimahmadov, I., 2020. The Tajik Basin: a composite record of sedimentary basin evolution in response to tectonics in the Pamir. Basin Research, doi: 10.1111/bre.12381.

Chapman, J.B., Robinson, A.C., Carrapa, B., Villarreal, D., Worthington, J., DeCelles, P.G., Kapp, P., Gadoev, M., Oimahmadov, I., Gehrels, G., 2018a. Cretaceous shortening and exhumation history of the South Pamir terrane. Lithosphere 10, 494-511.

Chapman, J.B., Scoggin, S.H., Kapp, P., Carrapa, B., Ducea, M.N., Worthington, J., Oimahmadov, I., Gadoev, M., 2018b. Mesozoic to Cenozoic magmatic history of the Pamir. Earth and Planetary Science Letters 482, 181-192.

Chen, S., Chen, H., 2020. Late Cenozoic Activity of the Tashkurgan Normal Fault and Implications for the Origin of the Kongur Shan Extensional System, Eastern Pamir. Journal of Earth Science 31, 723-734.

Clift, P.D., Zheng, H., Carter, A., Böning, P., Jonell, T.N., Schorr, H., Shan, X., Pahnke, K., Wei, X., Rittenour, T., 2017. Controls on erosion in the western Tarim Basin: Implications for the uplift of northwest Tibet and the Pamir. Geosphere 13, 1747-1765.

Coutand, I., Strecker, M., Arrowsmith, J., Hilley, G., Thiede, R., Korjenkov, A., Omuraliev, M., 2002. Late Cenozoic tectonic development of the intramontane Alai Valley,(Pamir - Tien Shan region, central Asia): An example of intracontinental deformation due to the Indo - Eurasia collision. Tectonics 21, 6, doi:10.1029/2002TC001358.

De Grave, J., Glorie, S., Ryabinin, A., Zhimulev, F., Buslov, M., Izmer, A., Elburg, M., Vanhaecke, F., 2012. Late Palaeozoic and Meso-Cenozoic tectonic evolution of the southern Kyrgyz Tien Shan: Constraints from multi-method thermochronology in the Trans-Alai, Turkestan-Alai segment and the southeastern Ferghana Basin. Journal of Asian Earth Sciences 44, 149-168.

Dedow, R., Franz, M., Szulc, A., Schneider, J.W., Brückner, J., Ratschbacher, L., Gągała, Ł., Ringenbach, J.C., Rajabov, N., Gadoev, M., 2020. Tajik Basin and Southwestern Tian Shan, Northwestern India - Asia Collision Zone: 3. Pre - to Syn - orogenic Retro - foreland Basin Evolution in the Eastern Tajik Depression and Linkage to the Pamir Hinterland. Tectonics 38, doi: 10.1029/2019TC005874.

Donelick, R.A., O'Sullivan, P.B., Ketcham, R.A., 2005. Apatite fission-track analysis. Reviews in Mineralogy and Geochemistry 58, 49-94.

Dumitru, T.A., Zhou, D., Chang, E.Z., Graham, S.A., Hendrix, M.S., Sobel, E.R., Carroll, A.R., 2001. Uplift, exhumation, and deformation in the Chinese Tian Shan. Geological Society of America Memoir 194, 71-99.

Gągała, Ł., Ratschbacher, L., Ringenbach, J.C., Kufner, S.K., Schurr, B., Dedow, R., Abdulhameed, S., Le Garzic, E., Gadoev, M., Oimahmadov, I., 2020. Tajik Basin and Southwestern Tian Shan, Northwestern India - Asia Collision Zone: 1. Structure, Kinematics, and Salt - tectonics in the Tajik Fold - and - thrust Belt of the Western Foreland of the Pamir. Tectonics 39, doi: 10.1029/2019TC005871.

Galbraith, R.F., 1981. On statistical models for fission track counts. Journal of the International Association for Mathematical Geology 13, 471-478.

Gallagher, K., Brown, R., Johnson, C., 1998. Fission track analysis and its applications to geological problems. Annual Review of Earth and Planetary Sciences 26, 519-572.

Garver, J.I., Brandon, M.T., Roden-Tice, M., Kamp, P.J.J., 1999. Exhumation history of orogenic highlands determined by detrital fission-track thermochronology. Geological Society, London, Special Publications 154, 283-304.

Gehrels, G.E., Valencia, V.A., Ruiz, J., 2008. Enhanced precision, accuracy, efficiency, and spatial resolution of U-Pb ages by laser ablation–multicollector–inductively coupled plasma–mass spectrometry. Geochemistry, Geophysics, Geosystems 9, Q03017, doi:10.1029/2007GC001805.

Gleadow, A.J.W., 1981. Fission-track dating methods: what are the real alternatives? Nuclear Tracks 5, 3-14.

Green, P., Duddy, I., Laslett, G., Hegarty, K., Gleadow, A.W., Lovering, J., 1989. Thermal annealing of fission tracks in apatite 4. Quantitative modelling techniques and extension to geological timescales. Chemical Geology: Isotope Geoscience Section 79, 155-182.

Hacker, B.R., Ratschbacher, L., Rutte, D., Stearns, M.A., Malz, N., Stübner, K., Kylander‐Clark, A.R., Pfänder, J.A., Everson, A., 2017. Building the Pamir‐Tibet Plateau—Crustal stacking, extensional collapse, and lateral extrusion in the Pamir: 3. Thermobarometry and Petrochronology of Deep Asian Crust. Tectonics 36, doi:10.1002/2017TC004488.

He, J., Kapp, P., Chapman, J.B., DeCelles, P.G., Carrapa, B., 2018. Structural setting and detrital zircon U–Pb geochronology of Triassic–Cenozoic strata in the eastern Central Pamir, Tajikistan. Geological Society, London, Special Publications 483, SP483. 411.

Heermance, R.V., Pearson, J., Moe, A., Langtao, L., Jianhong, X., Jie, C., Richter, F., Garzione, C.N., Junsheng, N., Bogue, S., 2018. Erg deposition and development of the ancestral Taklimakan Desert (western China) between 12.2 and 7.0 Ma. Geology 46, 919-922.

Imrecke, D.B., Robinson, A.C., Owen, L.A., Chen, J., Schoenbohm, L.M., Hedrick, K.A., Lapen, T.J., Li, W.Q., Yuan, Z.D., 2019. Mesozoic evolution of the eastern Pamir. Geosphere doi.org/10.1130/L1017.1.

Jepson, G., Carrapa, B., Gillespie, J., Feng, R., DeCelles, P.G., Kapp, P., Tabor, C.R., Zhu, J., 2021. Climate as the great equalizer of continental‐scale erosion. Geophysical Research Letters, e2021GL095008.

Jepson, G., Glorie, S., Konopelko, D., Mirkamalov, R., Danišík, M., Collins, A.S., 2018. The low-temperature thermo-tectonic evolution of the western Tian Shan, Uzbekistan. Gondwana Research 64, 122-136.

Jia, Y., Glotzbach, C., Lü, L., Ehlers, T.A., 2021. Cenozoic Tectono‐Geomorphologic Evolution of the Pamir‐Tian Shan Convergence Zone: Evidence From Detrital Zircon U‐Pb Provenance Analyses. Tectonics 40, e2020TC006345.

Kapp, P., DeCelles, P.G., 2019. Mesozoic–Cenozoic geological evolution of the Himalayan-Tibetan orogen and working tectonic hypotheses. American Journal of Science 319, 159-254.

Kaya, M.Y., Dupont‐Nivet, G., Proust, J.N., Roperch, P., Meijer, N., Frieling, J., Fioroni, C., Özkan Altiner, S., Stoica, M., Aminov, J., 2020. Cretaceous Evolution of the Central Asian Proto‐Paratethys Sea: Tectonic, Eustatic, and Climatic Controls. Tectonics 39, doi.org/10.1029/2019TC005983.

Ketcham, R.A., Donelick, R.A., Carlson, W.D., 1999. Variability of apatite fission-track annealing kinetics: III. Extrapolation to geological time scales. American Mineralogist 84, 1235-1255.

Klocke, M., Voigt, T., Kley, J., Pfeifer, S., Rocktäschel, T., Keil, S., Gaupp, R., 2017. Cenozoic evolution of the Pamir and Tien Shan Mountains reflected in syntectonic deposits of the Tajik Basin. Geological Society, London, Special Publications 427, 523-564.

Kufner, S.-K., Kakar, N., Bezada, M., Bloch, W., Metzger, S., Yuan, X., Mechie, J., Ratschbacher, L., Murodkulov, S., Deng, Z., 2021. The Hindu Kush slab break-off as revealed by deep structure and crustal deformation. Nature communications 12, 1-11.

Kufner, S.-K., Schurr, B., Sippl, C., Yuan, X., Ratschbacher, L., Ischuk, A., Murodkulov, S., Schneider, F., Mechie, J., Tilmann, F., 2016. Deep India meets deep Asia: Lithospheric indentation, delamination and break-off under Pamir and Hindu Kush (Central Asia). Earth and Planetary Science Letters 435, 171-184.

Leven, E.J., 1995. Permian and Triassic of the Rushan-Pshart Zone (Pamir). Riv. Ital. Paleontol. Stratigr 101, 3-16.

Li, L., Dupont-Nivet, G., Najman, Y., Kaya, M., Meijer, N., Poujol, M., Aminov, J., 2022. Middle to late Miocene growth of the North Pamir. Basin Research doi:10.1111/bre.12629.

Nielsen, S.B., Clausen, O.R., McGregor, E., 2017. basin% Ro: A vitrinite reflectance model derived from basin and laboratory data. Basin Research 29, 515-536.

Ogg, J.G., 2012. Geomagnetic Polarity Time Scale, in: Gradstein, F.M., Ogg, J.G., Schmitz, M., Ogg, G. (Eds.), The Geological Time Scale 2012. Elsevier, Amsterdam, pp. 85-113.

Peyton, S.L., Carrapa, B., 2013. An Introduction to Low-temperature Thermochronologic Techniques, Methodology, and Applications, in: Knight, C., Cuzella, J. (Eds.), Application of structural methods to Rocky Mountain hydrocarbon exploration and development. AAPG Studies in Geology 65, pp. 15-36.

Pozzi, J.-P., Feinberg, H., 1991. Paleomagnetism in the Tajikistan: Continental shortening of European margin in the Pamirs during Indian Eurasian collision. Earth and Planetary Science Letters 103, 365-378.

Reiners, P., Campbell, I., Nicolescu, S., Allen, C., Hourigan, J., Garver, J., Mattinson, J., Cowan, D., 2005. (U-Th)/(He-Pb) double dating of detrital zircons. American Journal of Science 305, 259-311.

Rembe, J., Sobel, E.R., Kley, J., Zhou, R., Thiede, R., Chen, J., 2021. The Carboniferous Arc of the North Pamir. Lithosphere 2021, 6697858.

Robinson, A.C., 2015. Mesozoic tectonics of the Gondwanan terranes of the Pamir plateau. Journal of Asian Earth Sciences 102, 170-179.

Robinson, A.C., Ducea, M., Lapen, T.J., 2012. Detrital zircon and isotopic constraints on the crustal architecture and tectonic evolution of the northeastern Pamir. Tectonics 31, doi:10.1029/2011TC003013,.

Robinson, A.C., Yin, A., Manning, C.E., Harrison, T.M., Zhang, S.-H., Wang, X.-F., 2004. Tectonic evolution of the northeastern Pamir: Constraints from the northern portion of the Cenozoic Kongur Shan extensional system, western China. Geological Society of America Bulletin 116, 953-973.

Ruiz, G.M.H., Seward, D., Winkler, W., 2004. Detrital thermochronology–a new perspective on hinterland tectonics, an example from the Andean Amazon Basin, Ecuador. Basin Research 16, 413-430.

Rutte, D., Ratschbacher, L., Khan, J., Stübner, K., Hacker, B.R., Stearns, M.A., Enkelmann, E., Jonckheere, R., Pfänder, J.A., Sperner, B., 2017a. Building the Pamir‐Tibetan Plateau—Crustal stacking, extensional collapse, and lateral extrusion in the Central Pamir: 2. Timing and rates. Tectonics 36, 385-419.

Rutte, D., Ratschbacher, L., Schneider, S., Stübner, K., Stearns, M.A., Gulzar, M.A., Hacker, B.R., 2017b. Building the Pamir‐Tibetan Plateau—Crustal stacking, extensional collapse, and lateral extrusion in the Central Pamir: 1. Geometry and kinematics. Tectonics 36, 342-384.

Schmidt, J., Hacker, B.R., Ratschbacher, L., Stübner, K., Stearns, M., Kylander-Clark, A., Cottle, J.M., Alexander, A., Webb, G., Gehrels, G., 2011. Cenozoic deep crust in the Pamir. Earth and Planetary Science Letters 312, 411-421.

Schneider, F., Yuan, X., Schurr, B., Mechie, J., Sippl, C., Haberland, C., Minaev, V., Oimahmadov, I., Gadoev, M., Radjabov, N., 2013. Seismic imaging of subducting continental lower crust beneath the Pamir. Earth and Planetary Science Letters 375, 101-112.

Schwab, M., Ratschbacher, L., Siebel, W., McWilliams, M., Minaev, V., Lutkov, V., Chen, F., Stanek, K., Nelson, B., Frisch, W., 2004. Assembly of the Pamirs: Age and origin of magmatic

belts from the southern Tien Shan to the southern Pamirs and their relation to Tibet. Tectonics 23, doi:10.1029/2003TC001583.

Searle, M., Hacker, B., 2018. Structural and metamorphic evolution of the Karakoram and Pamir following India–Kohistan–Asia collision. Geological Society, London, Special Publications 483, doi.org/10.1144/SP483.6.

Sippl, C., Schurr, B., Tympel, J., Angiboust, S., Mechie, J., Yuan, X., Schneider, F., Sobolev, S., Ratschbacher, L., Haberland, C., 2013. Deep burial of Asian continental crust beneath the Pamir imaged with local earthquake tomography. Earth and Planetary Science Letters 384, 165-177.

Sobel, E.R., Chen, J., Schoenbohm, L.M., Thiede, R., Stockli, D.F., Sudo, M., Strecker, M.R., 2013. Oceanic-style subduction controls late Cenozoic deformation of the Northern Pamir orogen. Earth and Planetary Science Letters 363, 204-218.

Sobel, E.R., Dumitru, T.A., 1997. Thrusting and exhumation around the margins of the western Tarim basin during the India-Asia collision. Journal of Geophysical Research 102, 5043-5063.

Sobel, E.R., Schoenbohm, L.M., Chen, J., Thiede, R., Stockli, D.F., Sudo, M., Strecker, M.R., 2011. Late Miocene–Pliocene deceleration of dextral slip between Pamir and Tarim: Implications for Pamir orogenesis. Earth and Planetary Science Letters 304, 369-378.

Sobel, E.R., Thiede, R., Ballato, P., Stübner, K., Kley, J., Rembe, J., Gadoev, M., Oimahmadov, I., Strecker, M., 2021. Uplift and growth of the northwest Pamir. EGU General Assembly Conference Abstracts EGU21-10405.

Stearns, M., Hacker, B., Ratschbacher, L., Rutte, D., Kylander‐Clark, A., 2015. Titanite petrochronology of the Pamir gneiss domes: Implications for middle to deep crust exhumation and titanite closure to Pb and Zr diffusion. Tectonics 34, 784-802.

Stearns, M.A., Hacker, B.R., Ratschbacher, L., Lee, J., Cottle, J.M., Kylander-Clark, A., 2013. Synchronous Oligocene–Miocene metamorphism of the Pamir and the north Himalaya driven by plate-scale dynamics. Geology 41, 1071-1074.

Stübner, K., Ratschbacher, L., Weise, C., Chow, J., Hofmann, J., Khan, J., Rutte, D., Sperner, B., Pfänder, J.A., Hacker, B.R., 2013. The giant Shakhdara migmatitic gneiss dome, Pamir, India - Asia collision zone: 2. Timing of dome formation. Tectonics 32, 1404-1431.

Sweeney, J.J., Burnham, A.K., 1990. Evaluation of a simple model of vitrinite reflectance based on chemical kinetics. AAPG bulletin 74, 1559-1570.

Tagami, T., 2005. Zircon fission-track thermochronology and applications to fault studies. Reviews in Mineralogy and Geochemistry 58, 95-122.

Taylor, G.H., Teichmüller, M., Davis, A., Diessel, C.F.K., Littke, R., Robert, P., 1998. Organic petrology. Schweizerbart Science Publishers, Berlin.

Thiede, R.C., Sobel, E.R., Chen, J., Schoenbohm, L.M., Stockli, D.F., Sudo, M., Strecker, M.R., 2013. Late Cenozoic extension and crustal doming in the India-Eurasia collision zone: New thermochronologic constraints from the NE Chinese Pamir. Tectonics 32, 763-779.

Thomas, J.C., Chauvin, A., Gapais, D., Bazhenov, M., Perroud, H., Cobbold, P., Burtman, V., 1994. Paleomagnetic evidence for Cenozoic block rotations in the Tadjik depression (Central Asia). Journal of Geophysical Research: Solid Earth 99, 15141-15160.

Vermeesch, P., 2018. IsoplotR: A free and open toolbox for geochronology. Geoscience Frontiers 9, 1479-1493.

Vermeesch, P., 2019. Statistics for Fission-Track Thermochronology, in: Malusà, M.G., Fitzgerald, P.G. (Eds.), Fission-Track Thermochronology and its Application to Geology. Springer International Publishing.

Villarreal, D.P., Robinson, A.C., Carrapa, B., Worthington, J., Chapman, J.B., Oimahmadov, I., Gadoev, M., MacDonald, B., 2020. Evidence for Late Triassic crustal suturing of the Central and Southern Pamir. Journal of Asian Earth Sciences: X 3, doi.org/10.1016/j.jaesx.2019.100024.

Wang, P., Liu, D., Li, H., Chevalier, M.-L., Wang, Y., Pan, J., Zheng, Y., Ge, C., Bai, M., Wang, S., 2021. Sedimentary Provenance Changes Constrain the Eocene Initial Uplift of the Central Pamir, NW Tibetan Plateau. Frontiers in Earth Science 9, doi: 10.3389/feart.2021.741194, 826.

Wang, X., Carrapa, B., Chapman, J.B., Henriquez, S., Wang, M., Decelles, P.G., Li, Z., Wang, F., Oimahmadov, I., Gadoev, M., 2019. Parathethys last gasp in central Asia and late Oligocene accelerated uplift of the Pamirs. Geophysical Research Letters 46, doi: https://doi.org/10.1029/2019GL084838.

Wang, X., Carrapa, B., Sun, Y.C., Dettman, D.L., Chapman, J.B., Rugenstein, J.K.C., 2020. The role of the westerlies and orography in Asian hydroclimate since the late Oligocene. Geology 48, 728-732.

Worthington, J.R., Ratschbacher, L., Stübner, K., Khan, J., Malz, N., Schneider, S., Kapp, P., Chapman, J.B., Stevens Goddard, A., Brooks, H.L., 2020. The Alichur dome, South Pamir, western India‐Asia collisional zone: detailing the Neogene Shakhdara‐Alichur syn‐collisional gneiss‐dome complex and connection to lithospheric processes. Tectonics 39, doi: 10.1029/2019TC005735.

Zanchi, A., Gaetani, M., 2011. The geology of the Karakoram range, Pakistan: the new 1: 100,000 geological map of Central-Western Karakoram. Italian Journal of Geosciences 130, 161-262.

Zhang, S.J., Hu, X.M., Garzanti, E., 2019. Paleocene initial indentation and early growth of the Pamir as recorded in the western Tarim Basin. Tectonophysics 772, doi.org/10.1016/j.tecto.2019.228207.

Zhang, Z., Sun, J., 2020. Cenozoic tectonic rotations in different parts of the NE Pamir: implications for the evolution of the arcuate orogen. International Journal of Earth Sciences 109, 1921-1939.

Zheng, H.B., Wei, X.C., Tada, R., Clift, P.D., Wang, B., Jourdan, F., Wang, P., He, M.Y., 2015. Late oligocene–early miocene birth of the Taklimakan Desert. Proceedings of the National Academy of Sciences 112, 7662-7667.

Figure captions

Figure 1. (A) Simplified tectonic map of the Pamir and surrounding regions, showing major terranes, suture zones (black curves), faults (red curves), rivers (blue curves), and gneiss domes (orange patches). Circles and stars represent sandstone and modern river sand samples, respectively: yellow, new samples of this study; blue, samples from earlier studies (Carrapa et al., 2014; Chapman et al., 2020; Wang et al., 2019). Abbreviations: KYTS, Kashgar-Yecheng transfer system; MPT, Main Pamir Thrust; RPS, Rushan-Pshart suture; TS, Taymas suture; TBZ, Tirich-Mir boundary zone. **Inset:** The dashed box shows the location of the main figure, TB, Tajik Basin; HK, Hindu Kush. **(B)** Geologic map of the study area, adapted from Dedow et al. (2020). Black solid curves are measured sections of this study: KH, Khirmanjo section; SB, Shurobod section; Black dashed curve is the previously studied section of Chapman et al. (2020): DH, Dashtijum section. Filled circles represent detrital samples for low-temperature thermochronology studies of this study (orange) and Chapman et al. (2020) (blue).

Figure 2. A simplified and composite stratigraphic section with information on the depositional environments of the studied KH and SB sections in the eastern Tajik Basin (KHN, KHP, and KHC represent the Neogene, Paleogene, and Cretaceous parts of the KH section). Stratigraphic ages and depositional environments are from Kaya et al. (2020) and Li et al. (2022). Note the long depositional hiatus between 37 and 20 Ma. The Global Polarity Time Scale (GPTS) is from Ogg (2012); the right column shows samples analyzed in this study.

Figure 3. Compilation of deconvolved AFT Peak Ages from sandstones from the eastern Tajik Basin and modern river sands from the Pamir. Horizontal gray bars are 1σ errors. Black arrows

indicate Peak Ages with <5% of single-grain AFT ages. P1–P5 are Peak Age populations shown in Table 2.

Figure 4. Compilation of deconvolved ZFT Peak Ages from sandstones from the eastern Tajik Basin and modern river sands from the Pamir. Horizontal gray bars are 1σ errors. Black arrows indicate Peak Ages with <5% of single-grain ZFT ages. P1–P5 are Peak Age populations shown in Table 3.

Figure 5. Kernel density estimate (KDE) plots (red curves) and histograms (vertical gray bars) of compiled AFT and ZFT Peak Ages. The upper panel (**A–B**) shows all data points (kernel bandwidth and histogram bin width are both 5 Ma) while the middle panel (**C–D**) shows <80 Ma data points (kernel bandwidth and histogram bin width are both 2 Ma).

Figure 6. Lag-time plots of **(A)** AFT Peak Ages and **(B)** ZFT Peak Ages of the KH & SB & DH sections of eastern Tajik Basin and modern river sands of the Pamir rivers. NP, CP, and SP represent the North, Central, and South Pamir, respectively.

Figure 7. Apatite U-Pb ages vs. AFT ages (**A**) and zircon U-Pb ages vs. ZFT ages (**B**) of the DH section. Each point represents a single grain.

Table 1. Information on newly analyzed samples from this study.

Sample[#]	Type	Stratigraphic heights[*] / m	Depositional Age / Ma	Latitude (°N)	Longitude (°E)	Analyses methods
18TJS03B	Sandstone	4421	8.0±0.3	37.83257	70.09195	AFT, Ap U-pb, ZFT
18TJS03A	Sandstone	4014	9.0±0.3	37.82774	70.08922	AFT, Ap U-Pb
18TJS02	Sandstone	3573	10.9±0.3	37.82588	70.10375	AFT, Ap U-Pb
TK16-1	Sandstone	3215	11.8±0.3	37.91050	70.11510	AFT, Ap U-Pb
TK18-42	Sandstone	3055	12.1±0.3	37.82238	70.11504	AFT, Ap U-Pb, ZFT
TK16-6	Sandstone	2953	12.4±0.3	37.91137	70.11865	AFT, Ap U-Pb, ZFT
TK16-11	Sandstone	2490	14.0±0.3	37.91246	70.12523	AFT, Ap U-Pb, ZFT
TK16-14	Sandstone	2070	16.3±0.3	37.91227	70.13194	AFT, Ap U-Pb, ZFT
TK16-18	Sandstone	1600	19.8±0.3	37.90847	70.13939	AFT, Ap U-Pb
18TJS07	Sandstone	1560	38±2 Ma	37.90783	70.14090	ZFT
TK16-28	Sandstone	880	92±2	37.90738	70.14846	AFT, Ap U-Pb
TK16-32	Sandstone	280	105±2	37.90621	70.15749	AFT, Ap U-Pb
TK18-44	Granite clast	2300	14.3±0.3	37.91255	70.12532	ZFT, Zr U-Pb
TK18-45	Granite clast	1850	18.0±0.3	37.90919	70.13778	ZFT, Zr U-Pb
TK16-35	Modern river sand	N.A.	0	38.46206	70.78967	AFT, Ap U-Pb, ZFT
TK16-36	Modern river sand	N.A.	0	38.29811	71.34425	AFT, Ap U-Pb, ZFT
TK16-37	Modern river sand	N.A.	0	38.19075	71.38169	AFT, Ap U-Pb
TK16-38	Modern river sand	N.A.	0	37.92667	71.59753	AFT, Ap U-Pb, ZFT
KRJ16-B-48	Shale	972	90±2	N.A.	N.A.	VF
KRJ16-B-49	Shale	965	90±2	N.A.	N.A.	VF
KRJ-16-B-31	Shale	568	97±2	N.A.	N.A.	VF
KRJ-16-B-P48	Shale	360	100±2	N.A.	N.A.	VF

Notes: AFT, apatite fission-track; ZFT, zircon fission-track; Ap, apatite; Zr, zircon; VF, vitrinite reflectance; N.A. not available.

[#] See Fig. 1 for locations on map.

[*] See Fig. 2 for stratigraphic heights.

Table 2. Deconvolved Peak Ages for detrital apatite fission-track data from newly collected samples and published data.

Sample	Depositional Age / Ma	N	P1*	P2*	P3*	P4*	P5*	Others*
KH & SB section sandstones, eastern Tajik Basin, this study								
18TJS03B	8.0±0.3	50	-	-	60.0±4.8 (39%)	136.6±6.6 (61%)	-	-
18TJS03A	9.0±0.3	56	-	19.5±5.5 (10%)	-	131.0±2.8 (90%)	-	-
18TJS02	10.9±0.3	49	-	25.1±2.3 (23%)	61.0±4.3 (26%)	120.1±4.4 (51%)	-	-
TK16-1	11.8±0.3	67	-	-	56.5±3.4 (26%)	108.9±3.7 (46%)	203.3±10.2 (28%)	-
TK18-42	12.1±0.3	65	-	20.9±2.7 (12%)	46.9±3.1 (24%)	93.7±2.9 (42%)	160.8±7.2 (22%)	-
TK16-6	12.4±0.3	78	-	21.6±3.2 (8%)	-	93.3±2.7 (53%)	160.1±5.5 (39%)	-
TK16-11	14.0±0.3	72	11.2±1.7 (6%)	-	44.2±3.1 (10%)	94.8±3.3 (39%)	-	137.1±4.7 (45%)
TK16-14	16.3±0.3	83	-	17.2±0.9 (57%)	66.4±3.3 (21%)	114±3.1 (22%)	-	-
TK16-18	19.8±0.3	55	-	27.8±2.2 (54%)	-	109.3±2.9 (46%)	-	-
TK16-28	92±2	70	5.7±1.7 (12%)	-	50.4±3.2 (46%)	110.9±3.0 (42%)	-	-
TK16-32	105±2	54	7.1±0.5 (69%)	30.0±2.7 (19%)	84.0±4.5 (12%)	-	-	-
Modern river sands, western Pamir, this study†								
TK16-35 (NP)	0	66	13.4 (55%)	24.8 (45%)	-	-	-	-
TK16-36 (CP)	0	67	9.3±0.6 (87%)	22.0±2.4 (13%)	-	-	-	-
TK16-37 (CP)	0	43	6.3±0.5 (50%)	-	-	-	-	15.3±1.7 (50%)
TK16-38 (CP/SP)	0	31	6.9±0.8 (84%)	22.1±5.7 (16%)	-	-	-	-
Modern river sands, Pamir, reprocessed data from Carrapa et al. (2014)†								
TJK4 (CP)	0	100	14.4±0.7 (69%)	25.3±2.1 (30%)	-	-	161.7±65.4 (1%)	-
TJK5 (SP)	0	102	11.0±0.6 (60%)	16.7±1.2 (38%)	-	103.2±18.7 (2%)	-	-
TJK6 (CP/SP)	0	100	-	16.9±0.5 (100%)	-	-	-	-
TJK7 (CP)	0	100	11.7±0.5 (59%)	27.2±1.4 (36%)	86.4±7.2 (5%)	-	-	-
TJK8 (CP)	0	100	15.3±0.6 (76%)	35.7±3.0 (23%)	-	130.3±42.0 (1%)	-	-
1071-1 (NP)	0	100	13.2±1.1 (13%)	22.5±1.5 (37%)	-	-	-	35.5±1.4 (50%)
1071-2 (NP)	0	100	6.7±0.5 (39%)	33.5±1.4 (35%)	-	-	-	16.5±2.1 (26%)
1071-3 (NP)	0	100	6.8±0.7 (26%)	-	44.7±3.5 (16%)	-	-	15.1±0.9 (59%)
1071-4 (NP)	0	100	-	22.2±0.6 (100)	-	-	-	-
1071-6 (NP)	0	42	12.5±1.1 (43%)	26.1±1.9 (45%)	86.8±9.3 (12%)	-	-	-
1071-7 (NP)	0	100	12.9±0.7 (66%)	23.3±1.6 (35%)	-	-	-	-

Note: N, number of grains accepted; P1–P5 are Peak Age Populations, which group similar FT Peak Ages together. When there is more than one Peak Ages that fell into a specific population, the Peak Age with a smaller percentage of single-grain ages was categorized as "Others".

* Numbers in brackets represent percentages of single-grain ages in each sample. Dividing the percentages by 10 and then rounding them to their nearest integer derive the weights of individual Peak Ages (0 to 10) as discussed in section 3.4.2 (e.g., 39% would derive a weight of 4).

† NP/CP/SP, indicates rivers draining the North, Central, and South Pamir respectively.

Table 3. Deconvolved Peak Ages for detrital zircon fission-track data from newly collected samples and published data.

Sample	Depositional Age / Ma [#]	N	P1[*]	P2[*]	P3[*]	P4[*]	P5[*]	Others[*]
KH & SB section sandstones, eastern Tajik Basin, this study								
18TJS03B	8.0±0.3	20	-	-	73.6±22.8 (10%)	-	217.9±12.9 (90%)	-
TK18-42	12.1±0.3	20	9.6±4.8 (5%)	-	82.6±13.0 (18%)	-	228.1±15.2 (77%)	-
TK16-6	12.4±0.3	27	-	-	-	101.4±6.2 (82%)	-	266.8±39.6 (18%)
TK16-11	14.0±0.3	40	-	37.8±5.5 (8%)	-	90.8±3.6 (70%)	215.5±18.9 (22%)	-
TK16-14	16.3±0.3	36	-	35.2±3.0 (21%)	61.0±2.4 (79%)	-	-	-
18TJS07	38±2 Ma	20	-	-	68.4±5.9 (56%)	-	-	359.8±59.9 (44%)
KH section granite clasts, eastern Tajik Basin, this study								
TK18-44	14.3±0.3	20	-	-	-	-	-	272.3±18.0 (100%)
TK18-45[‡]	18.0±0.3	18	-	-	-	-	212.3±14.7 (100%)	-
Modern river sands, western Pamir, this study[†]								
TK16-35 (NP)	0	61	-	18.2±2.0 (13%)	70.3±8.8 (36%)	135.5±9.4 (51%)	-	-
TK16-36 (CP)	0	35	11.5±1.5 (27%)	24.2±2.0 (56%)	52.5±5.3 (14%)	-	211.0±66.2 (3%)	-
TK16-38 (CP/SP)	0	56	-	18.6±1.4 (56%)	-	-	194.9±17.3 (16%)	35.5±3.1 (28%)
DH section sandstones, eastern Tajik Basin, reprocessed data from Chapman et al. (2020)								
DSH5090	7.5±1.0	90	-	16.2±0.8 (38%)	41.1±3.3 (11%)	92.2±4.1 (31%)	204.5±10 (20%)	-
DSH3469	13.0±1.0	57	-	20.0±1.5 (22%)	-	95.5±3.1 (61%)	180.0±10.2 (17%)	-
DSH3164	13.5±1.0	109	-	24.7±1.3 (20%)	-	101.2±2.7 (61%)	226.9±10.5 (19%)	-
DSH2566	17.0±1.0	91	-	31.3±1.9 (20%)	-	108.7±5.0 (59%)	203.4±14.0 (21%)	-
DSH2225	17.5±1.0	83	-	27.5±1.1 (42%)	-	96.0±3.8 (45%)	-	162.9±13.1 (13%)
DSH470	100±3.0	87	-	-	-	103.0±2.9 (76%)	204.4±11.6 (24%)	-

Note: N, number of grains accepted; P1–P5, Peak Age Populations, see definition in Table 2.

[*] Numbers in brackets represent percentages of single-grain ages in each sample. Dividing the percentages by 10 and then rounding them to their nearest integer derive the weights of individual Peak Ages (0 to 10) as discussed in section 3.4.2 (e.g., 10% would derive a weight of 1).

[#] Depositional ages of the DH section were determined by correlating the DH section with the adjacent magnetostratigraphically dated KH and SB sections from Li et al. (2022).

[†] See Table 2 for the draining terranes of the modern river sand samples.

[‡] See Supplementary Text S4 for further discussion.

Table 4. Vitrinite reflectance (% Ro) data of shales from the Cretaceous strata in the KH section.

Sample ID	Stratigraphic height (m)*	Approximate age (Ma)#	Number of analysis	Ro (%)	S.D.	Temp. (°C)[1]	Temp. (°C)[2]
KRJ16-B-48	972	90±2	50	0.50	0.13	70	90
KRJ16-B-49	965	90±2	39	0.44	0.13	54	80
KRJ-16-B-31	568	97±2	51	0.67	0.17	106	114
KRJ-16-B-P48	360	100±2	34	0.61	0.13	94	107

Note: S.D. Standard deviation; Temp. Temperature.

* See Figure 2 for stratigraphic heights.

Approximate ages are derived from Kaya et al. (2020).

[1] Temperature estimated from Barker and Goldstein (1990): $T(°C) = (\ln(\%Ro) + 1.26)/0.00811$.

[2] Temperature estimated from Sweeney and Burnham (1990): $T(°C) = 82.529 * \ln(\%Ro) + 147.51$.

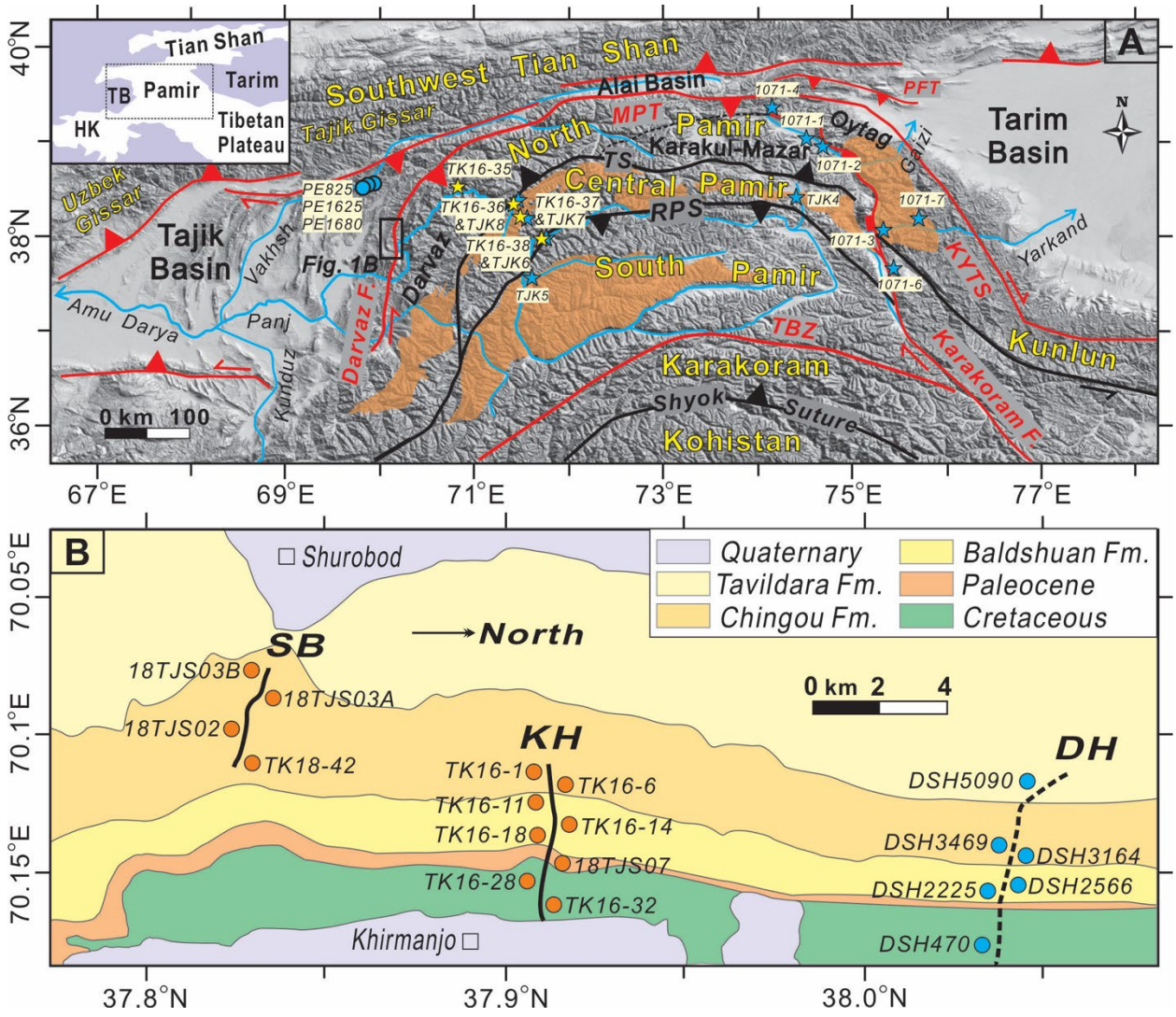

Figure 1

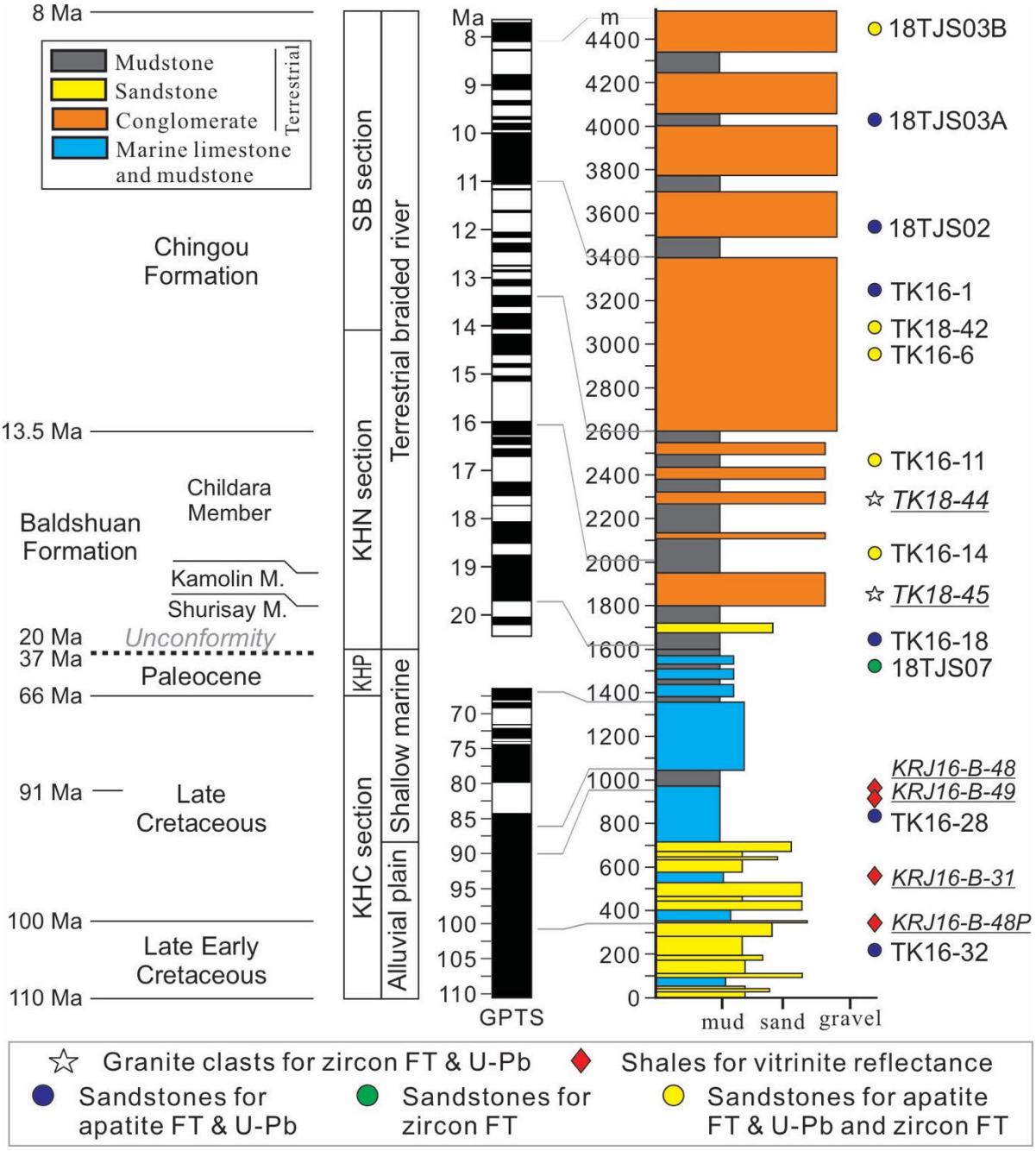

Figure 2

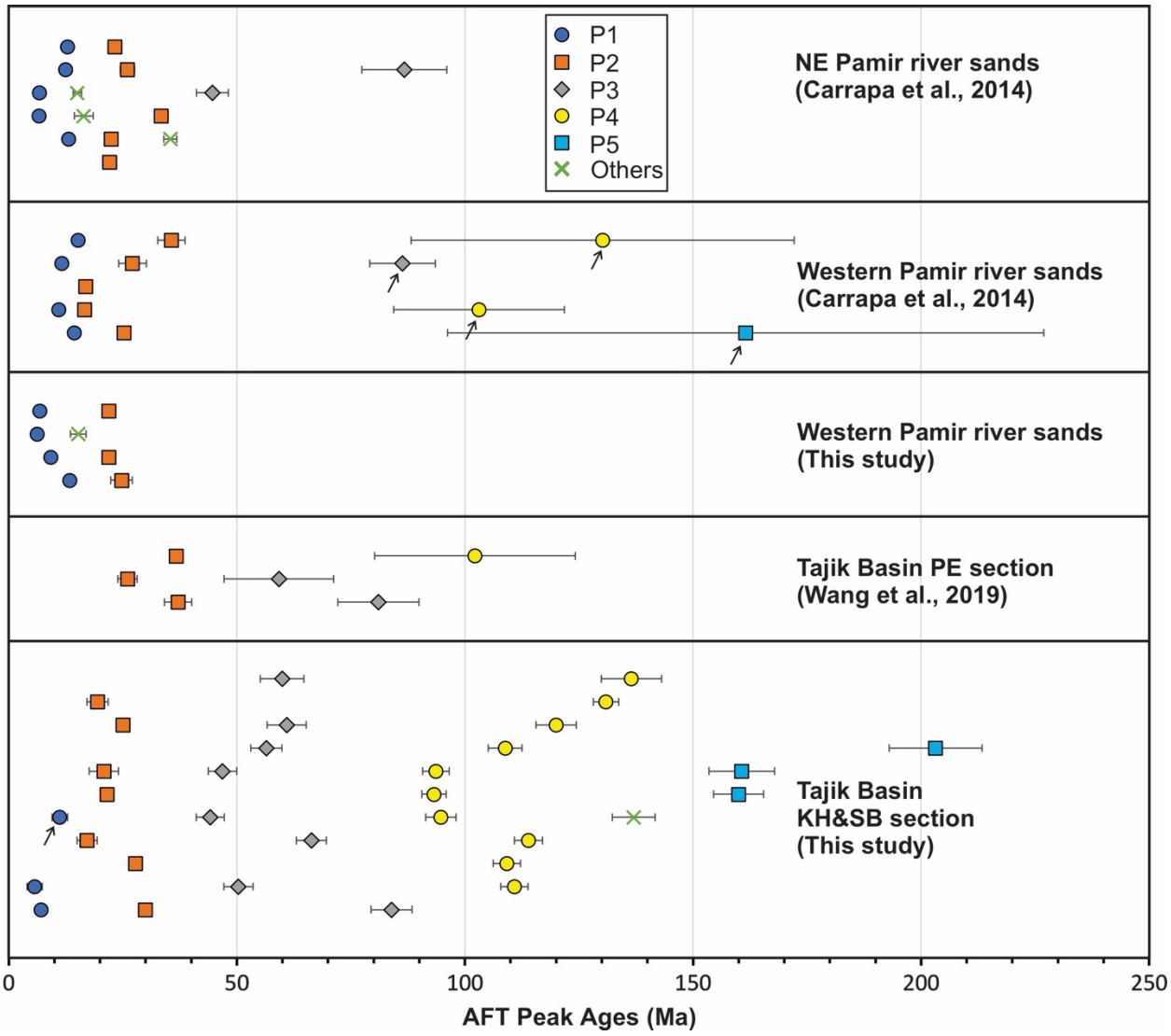

Figure 3

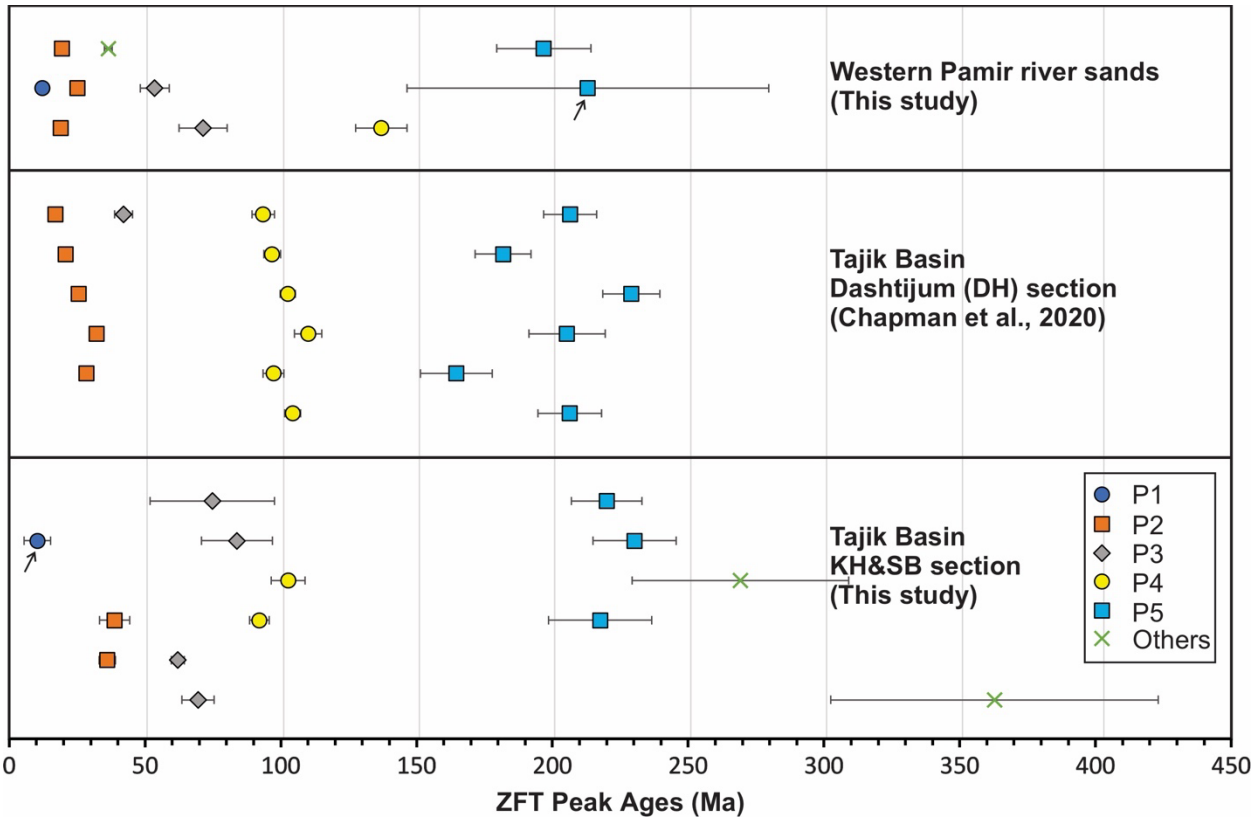

Figure 4

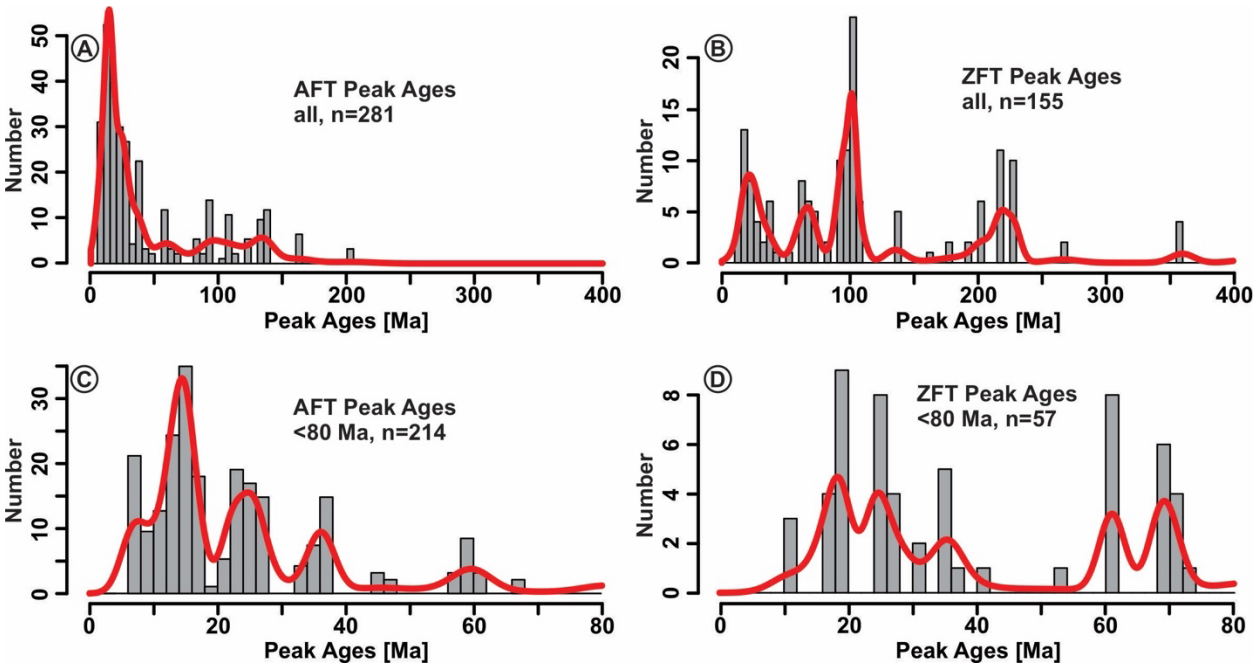

Figure 5

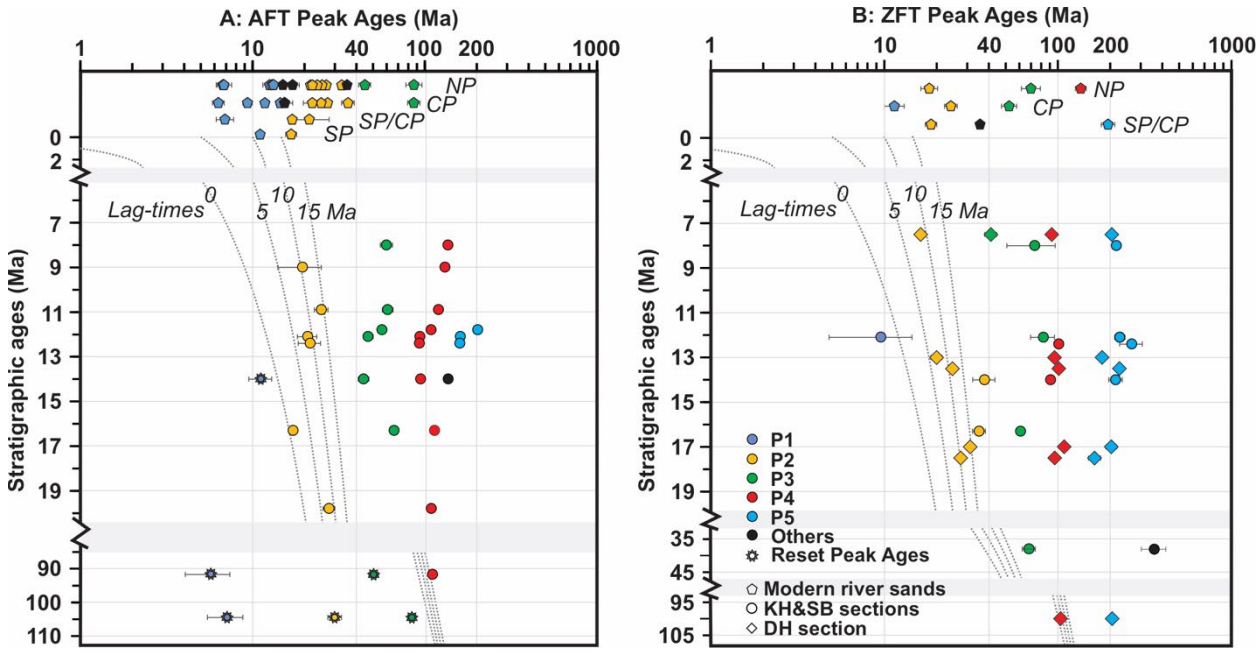

Figure 6

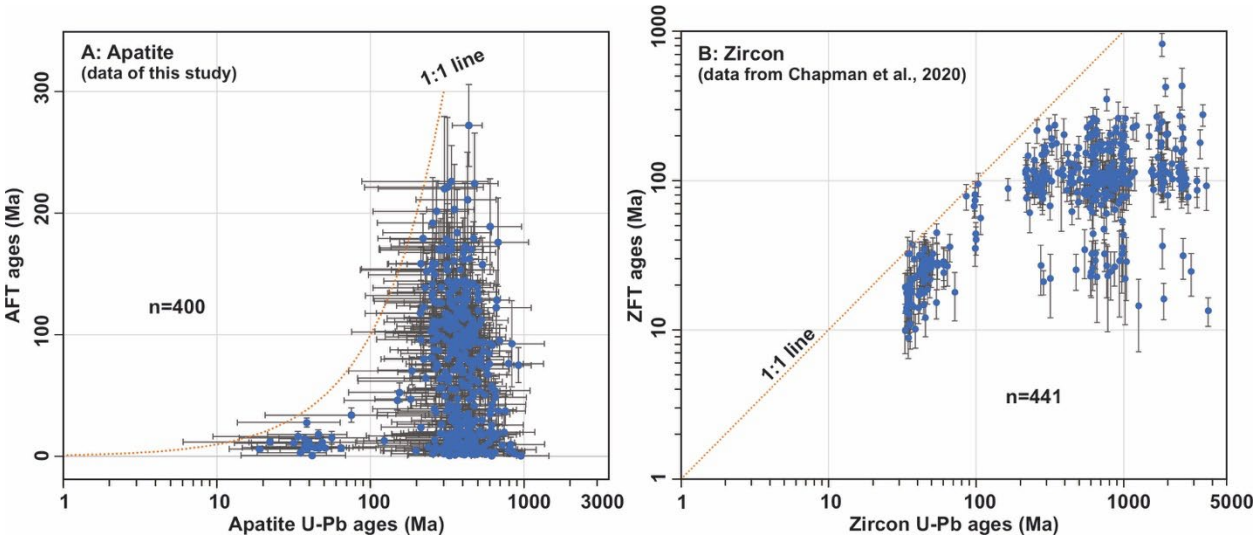

Figure 7